Paleoceanography and Paleoclimatology

RESEARCH ARTICLE
10.1029/2018PA003441

Key Points:
- The predicted carbon isotopes of dissolved inorganic carbon (DIC) in the modern surface waters display latitudinal variability related to biological uptake and air-sea exchange of CO_2
- Preindustrial carbon isotopes and planktic foraminifera *Globigerina bulloides* temperature corrected from core tops in the subtropical and subantarctic surface waters are substantially higher than modern Carbon isotopes of DIC, due to the Suess Effect
- Downcore carbon isotopes of G. bulloides show large variations linked to a combination of productivity, air-sea CO_2 exchange, and ocean circulation, likely influenced by variations in the Southern Hemisphere Westerly Wind structure over the last 25 kyr

Supporting Information:
- Supporting Information S1
- Table S1
- Table S2
- Table S3

Correspondence to:
H. Bostock,
helen.bostock@niwa.co.nz

Citation:
Maxson, C., Bostock, H., Mackintosh, A., Mikaloff-Fletcher, S., McCave, N., & Neil, H. (2019). Modern, preindustrial, and past (last 25 ka) carbon isotopic ($\delta^{13}C$) variability in the surface waters of the southwest Pacific. *Paleoceanography and Paleoclimatology*, *34*, 692–714. https://doi.org/10.1029/2018PA003441

Received 25 JUL 2018
Accepted 29 MAR 2019
Accepted article online 3 APR 2019
Published online 30 APR 2019

Modern, Preindustrial, and Past (Last 25 ka) Carbon Isotopic ($\delta^{13}C$) Variability in the Surface Waters of the Southwest Pacific

Charles R. Maxson[1], Helen C. Bostock[2], Andrew Mackintosh[1], Sara Mikaloff-Fletcher[2], Nick McCave[3], and Helen L. Neil[2]

[1]Antarctic Research Centre, Victoria University, Wellington, New Zealand, [2]National Institute of Water and Atmospheric Research, Wellington, New Zealand, [3]Department of Earth Sciences, University of Cambridge, Cambridge, UK

Abstract Carbon stable isotopes ($\delta^{13}C$) in modern seawater samples and planktic foraminifera *Globigerina bulloides* from core top and downcore sediments are used to estimate the distribution of $\delta^{13}C$ of dissolved inorganic carbon (DIC) in the surface waters of the southwest Pacific in the modern, preindustrial (PI), and over the last 25 kyr. The predicted $\delta^{13}C$ distribution in the modern ($\delta^{13}C_{DIC}$), PI ($\delta^{13}C_{PI}$), and late Holocene (from planktic foraminifera *Globigerina bulloides* [temperature corrected $\delta^{13}C_{G.\ bulloides TC}$] from core tops) displays a broad peak at the subtropical front) and subantarctic surface waters due to the combination of high biological productivity and thermodynamic air-sea gas exchange of CO_2 in this region. The estimated $\delta^{13}C_{PI}$ values and measured $\delta^{13}C_{G.bulloides TC}$ values from the core tops are higher than the modern values due to the Suess Effect. However, there is poor agreement between the $\delta^{13}C_{PI}$ values and core top $\delta^{13}C_{G.bulloides TC}$ values south of 40°S as the back-calculation approach using chlorofluorocarbon-11 (CFC-11) method for removing the anthropogenic $\delta^{13}C$ is not effective at these higher southern latitudes. The $\delta^{13}C_{G.bulloides TC}$ from a latitudinal transect of cores in the southwest Pacific were compiled by region using a Monte Carlo approach to determine the long-term trends in $\delta^{13}C$ over the last 25 kyr. Glacial subantarctic $\delta^{13}C_{G.bulloides TC}$ values are low, while subtropical $\delta^{13}C_{G.bulloides TC}$ are high. The peak in $\delta^{13}C_{G.bulloides TC}$ values shifts south in the early Holocene. These latitudinal variations in $\delta^{13}C_{G.\ bulloides TC}$ are linked to changes in ocean circulation, biological productivity (associated with the shifts in the subtropical front), and air-sea CO_2 exchange, likely related to the structure and position of the Southern Hemisphere Westerly Wind in the South Pacific region.

1. Introduction

The exchange of carbon, via carbon dioxide (CO_2), between the ocean and atmosphere is the primary process proposed to drive glacial/interglacial cycles. The exact mechanisms of how this occurs are still up for debate, but the current consensus is that it primarily exchanges in the Southern Ocean (Anderson et al., 2009; Gottschalk et al., 2015). Stable carbon isotopes ($\delta^{13}C$) in the surface waters can potentially provide information about the exchange of carbon between the ocean and the atmosphere if the different processes that influence $\delta^{13}C$ can be unraveled. Carbon isotopes ($\delta^{13}C_{DIC}$) in the surface waters of the ocean are influenced by three different processes: biological productivity, air-sea exchange of CO_2 (affected by thermodynamic processes), and circulation (Charles & Fairbanks, 1990; Kroopnick, 1985; Lynch-Stieglitz et al., 1995; Schmittner et al., 2013). Biological productivity results in the increase in $\delta^{13}C$ in the dissolved inorganic carbon (DIC) in the surface waters of the ocean as photosynthesis by phytoplankton preferentially takes up the lighter ^{12}C (Kroopnick, 1985). Air-sea exchange of CO_2 causes an enrichment of $\delta^{13}C_{DIC}$ at cold temperatures but depletion of $\delta^{13}C_{DIC}$ in warm temperatures (Lynch-Stieglitz & Fairbanks, 1994; Lynch-Stieglitz et al., 1995; Mook et al., 1974; Ninnemann & Charles, 1997; Zhang et al., 1995). Ocean circulation alters the $\delta^{13}C_{DIC}$ through processes such as upwelling of ^{12}C-enriched deep waters (lowering the $\delta^{13}C_{DIC}$) or horizontal mixing with other water masses but also through variations in the residence time of the water mass at the surface (i.e., if the water mass sits at the surface for sufficient time, it will have long enough to develop temperature-dependent air-sea isotopic fractionation [as mentioned above]). Measurements and models of $\delta^{13}C_{DIC}$, in conjunction with other hydrographic data (temperature, oxygen, and phosphate), have provided insight into the dominance of these three main processes in different regions of the modern ocean (Gruber et al., 1999; Lynch-Stieglitz et al., 1995; Schmittner et al., 2013). Moreover, $\delta^{13}C_{DIC}$ data collected over

50 years show that the isotopic values in the surface waters have been declining over the past half century as a result of the "Suess Effect" (Gruber et al., 1999; Keeling, 1979; McNeil et al., 2001; Quay et al., 1992, 2003, 2009; Quay et al., 2007; Sonnerup et al., 1999), although the rates of oceanic uptake of the anthropogenic CO_2 vary depending on thermodynamics, pH, and ocean circulation (Gruber et al., 1999; Ko et al., 2016; Sabine et al., 2004).

In theory by measuring the $\delta^{13}C$ from planktic foraminifera from marine sediment cores we can determine past changes in the $\delta^{13}C_{DIC}$ of the surface waters, to help elucidate the exchange of carbon between the ocean and the atmosphere and the global carbon cycle. In practice there are many complicating factors in deciphering the $\delta^{13}C_{foram}$ signal. The relationship between $\delta^{13}C_{foram}$ and $\delta^{13}C_{DIC}$ is commonly affected by biological vital effects and may vary spatially or be poorly understood (Gottschalk et al., 2015; Kohfeld et al., 2000), and it is hard to deconvolve the different factors affecting the $\delta^{13}C_{DIC}$ (air-sea gas exchange of CO_2, biological productivity, and ocean circulation—discussed above) over glacial/interglacial cycles. Previous studies have used $\delta^{13}C_{foram}$ from marine sediment cores to suggest a strong relationship between the surface water $\delta^{13}C_{DIC}$ and atmospheric $\delta^{13}C$ (measured in the ice cores), indicating that carbon exchange between the oceans and the atmosphere plays a dominant role in global climate change over the deglaciation (Anderson et al., 2009; Bostock et al., 2004; Charles et al., 1996; Martínez-Botí et al., 2015; Spero & Lea, 2002). Other studies have used the $\delta^{13}C_{foram}$ records to show changes in biological productivity and nutrients in the Southern Ocean (Hodell et al., 2000; Ninnemann & Charles, 1997) or suggested that changes in ocean circulation and stratification are the dominant control on the glacial/interglacial $\delta^{13}C_{foram}$ records (Carter et al., 2008; Neil et al., 2004; Nelson et al., 1993, 2000; Schiraldi et al., 2014). Alternatively, it is a combination of all of these factors, as recently suggested by Gottschalk et al. (2015) for the deglaciation in the Subantarctic Zone of the South Atlantic. They suggested that, after corrections for known biological vital effects, the changes in planktic $\delta^{13}C_{foram}$ (*Globigerina bulloides* and *Neogloboquadrina pachyderma*) reflect changes in the ocean circulation due to shifting of the fronts, changes in the efficiency of air-sea gas exchange due to surface ocean density stratification and sea ice, and changes in biological productivity, which all influence the $\delta^{13}C_{foram}$ and the CO_2 exchange and between the surface waters of the Southern Ocean and the atmosphere.

In this study we aim to improve the current understanding of $\delta^{13}C_{DIC}$ and $\delta^{13}C_{PI}$ of the surface waters of the subtropical to subantarctic of the undersampled southwest Pacific and the primary processes controlling them. The $\delta^{13}C_{PI}$ was estimated (by attempting to remove the Suess Effect) to understand the thermodynamic air-sea gas exchange of CO_2 since the PI and also to compare to the temperature corrected $\delta^{13}C$ of the planktic foraminifera *G. bulloides* ($\delta^{13}C_{G.bulloidesTC}$) of the core tops to ensure that the vital effects had been removed. This understanding of the predicted $\delta^{13}C_{DIC}$ and $\delta^{13}C_{PI}$ and the main processes affecting them were then used to interpret the changes in $\delta^{13}C_{G.bulloidesTC}$ from a latitudinal transect of cores to understand past changes in biological productivity, air-sea gas exchange of CO_2, and ocean circulation in the southwest Pacific since the last glacial (25 kyr) and how these relate to the global climate changes over this time period (Figure 1).

1.1. Modern Oceanography

In this section, we summarize the main surface water fronts and currents and water masses and their characteristics from the World Ocean Atlas (2013; Figures 2a–2d), including their measured $\delta^{13}C_{DIC}$ signatures determined from the World Ocean Circulation Experiment (WOCE) transects, for the southwest Pacific, and Southern Ocean (Figure 2e and Table 1).

The subtropical surface waters (STSW) of the subtropical gyre are defined as waters with a potential temperature >15 °C (Chiswell et al., 2015) and are the most saline water in the region with a salinity >35 psu with very low nutrient concentrations (phosphate <0.25 μmol/kg). The $\delta^{13}C_{DIC}$ values in STSW display a large range from 1.1‰ to 1.5‰ and increasing to almost 2‰ close to the subtropical front (STF; 40–45°S; Table 1 and Figure 2). The STF is the boundary between the warm, salty, nutrient-poor STSW of the subtropical gyre and the cool (6–12 °C), fresh (34.3–34.5 psu), nutrient-rich (phosphate 0.5–1 μmol/kg) subantarctic surface waters (SASW; Chiswell et al., 2015; Tomczak & Godfrey, 1994; Table 1). The STF typically sits between 40°S and 45°S in most of the Southern Ocean but is forced south to 49.5°S by the complex and shallow topography around New Zealand (Smith et al., 2013). In the open ocean, the STF is wide zone, slow, and diffuse, with no flow associated with it, as it extends across the Tasman Sea (Hamilton, 2006) and main South Pacific

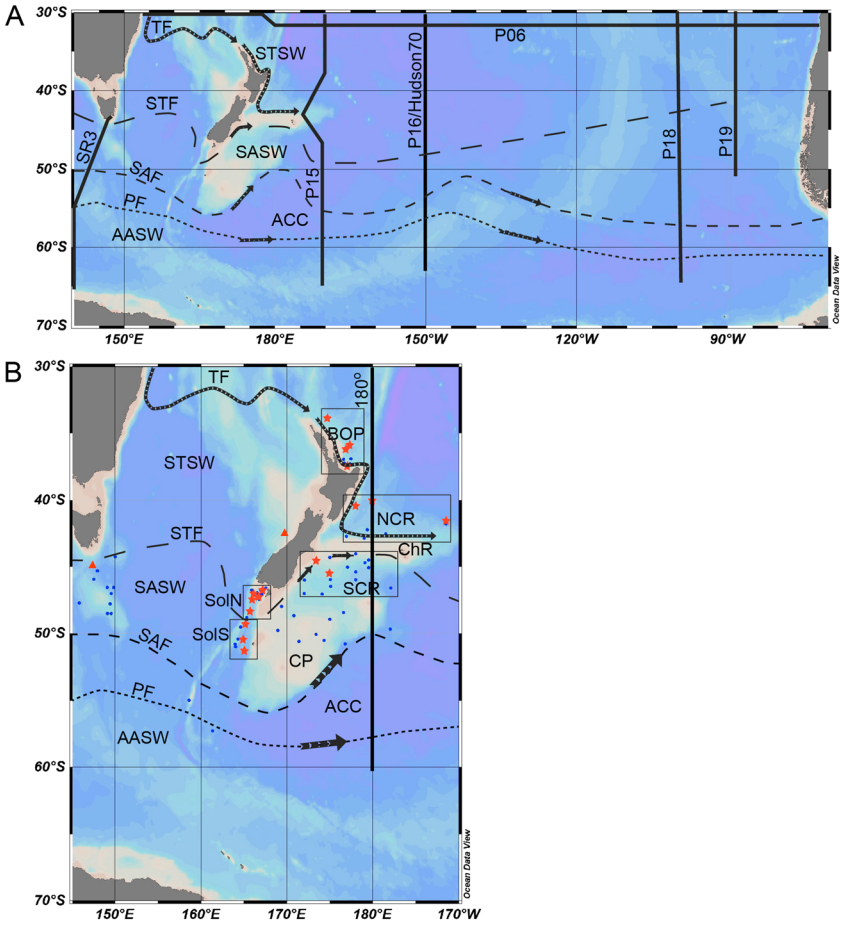

Figure 1. (a) South Pacific map showing the location of the WOCE transects (Table 2 and supporting information Table S2) and the main fronts in the southwest Pacific. (b) Local circulation and surface water masses and the location of all core tops (blue dots) and cores (red stars) used in this study from the southwest Pacific. Red triangles show the location of the benthic $\delta^{13}C_{C.wuellerstorfi}$ cores GC34 (Lower Circumpolar Deep Water; Moy et al., 2006) and SO136-03 (Antarctic Intermediate Water; Ronge et al., 2015). Black boxes show the five main regions studied in this paper: BOP = Bay of Plenty; NCR = North Chatham Rise; SCR = South Chatham Rise; SolN = Solander Trough, North; SolS = Solander Trough, South. ChR = Chatham Rise, CP = Campbell Plateau. The main surface water masses and fronts are labeled. STSW = Subtropical Waters; SASW = Subantarctic Waters; AASW = Antarctic Surface Waters; TF = Tasman Front; STF = Subtropical Front (black long dashes); SAF = Subantarctic Front (black medium dashes); PF = Polar Front (black short dashes). Black arrows indicate the main flow within the Antarctic Circumpolar Current (ACC) that occurs within the SAF and PF. Adapted from Sokolov & Rintoul, 2009a, 2009b, using the mean position of the Southern Ocean fronts, and Chiswell et al., 2015. Figure made in ODV (Schlitzer, 2009).

basins (Graham & de Boer, 2013). In contrast at the edge of the basins, such as east of New Zealand, the STF is a narrow, strong dynamic front (dynamic STF; Chiswell et al., 2015; Graham & de Boer, 2013; Smith et al., 2013). Mixing across the STF creates a region of high biological productivity due to the presence of both micronutrient and macronutrient from the north (STSW) and south (SASW), respectively. The high biological productivity in this region is reflected in the highest $\delta^{13}C_{DIC}$ values ranging from 1.75‰ to 2.25‰ in the SASW.

The Subantarctic Front (SAF) forms the northern boundary of the Antarctic Circumpolar Current (ACC). The SAF has multiple jets that transport most of the water in the ACC. The position of the SAF is strongly controlled by the topography of the region, being forced through gaps in the Macquarie Ridge and south around the Campbell Plateau (Sokolov & Rintoul, 2009a, 2009b). The PF is also deflected by the topography and is made up of multiple jets that are associated with most of the flow. The polar front (PF) is associated with significant upwelling of cold, nutrient-rich Circumpolar Deep Waters (CDW) with low $\delta^{13}C_{DIC}$ 0.5–0.6‰ (Table 1). To the south of the PF, Antarctic Surface Waters (AASW) are <34 psu with temperatures of −2–1 °C with $\delta^{13}C_{DIC}$ of 0.5–0.75‰.

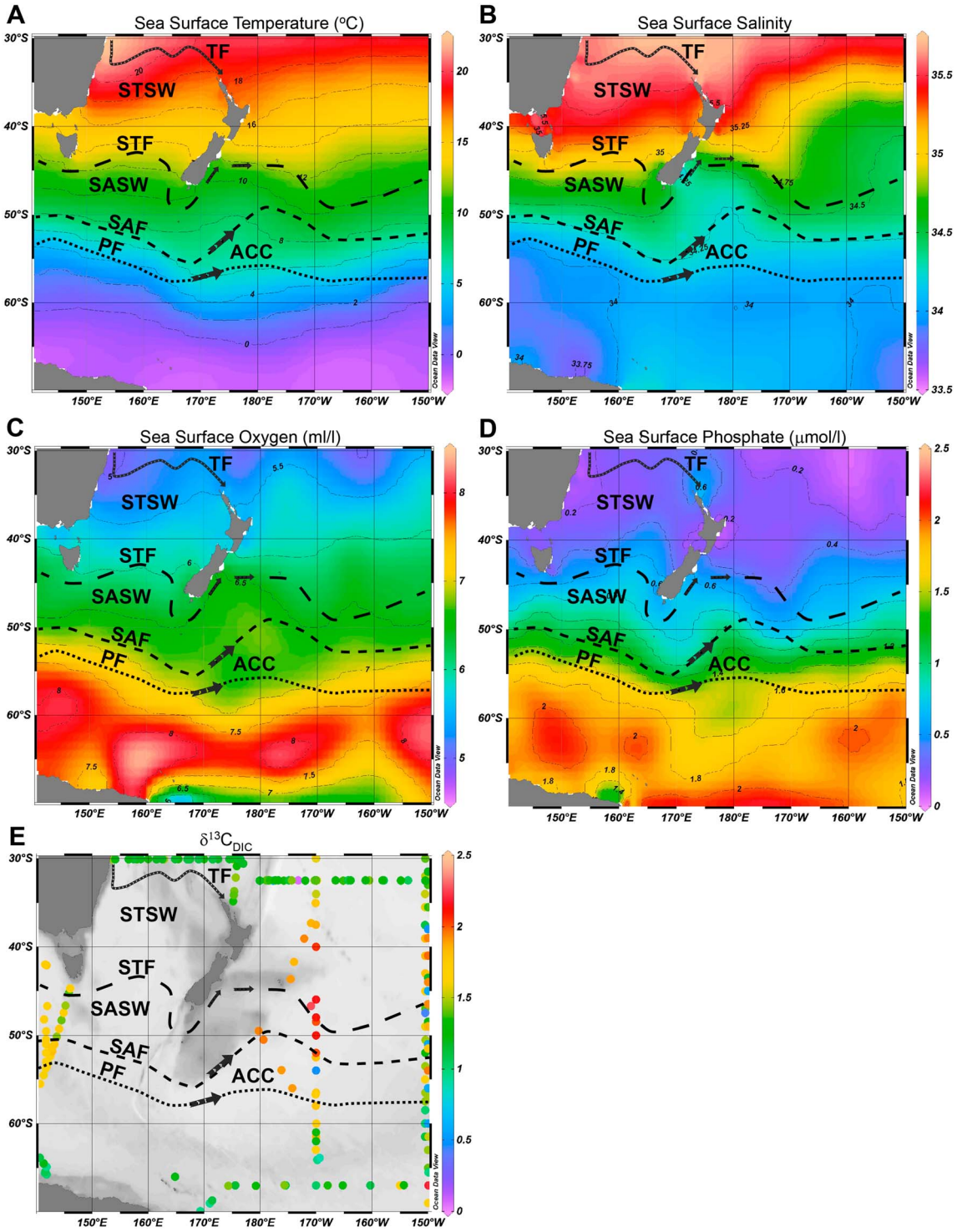

Figure 2. Surface water properties of the southwest Pacific from World Ocean Atlas (2013). (a) Sea surface temperature, (b) sea surface salinity, (c) sea surface oxygen, (d) sea surface phosphate, and (e) $\delta^{13}C_{DIC}$ measured on World Ocean Circulation Experiment transects. Figure made in ODV (Schlitzer, 2009). Position of the fronts and currents adapted from Chiswell et al. (2015). TF = Tasman Front; STSW = Subtropical Waters; STF = Subtropical Front; SASW = Subantarctic Waters; SAF = Subantarctic Front; PF = Polar Front; ACC = Antarctic Circumpolar Current.

Table 1
Water Mass Properties From Voyages SR3, P15, P16, and P18

Water mass	Depth range (m)	Latitude (°S)	Potential temperature (°C)	Salinity (psu)	AOU (μmol/kg)	Phosphate (μmol/kg)	$\delta^{13}C_{DIC}$ (‰)
STSW	0–200	<40	>15	>34.8	−20 to 0	<0.25	1–1.9
SASW	0–200	40–53	6–12	34.3–34.5	0–10	0.5–1	1.75–2.25
AASW	0–200	>55	−2 to 2	<34	10–50	1.5–1.75	0.5–1.5
SAMW	200–500	<55	8–10	34.4–34.75	20–50	1–1.5	1.25–1.5
AAIW	500–1,500	<55	4–8	34.3–34.5	50–130	1.5–2.4	0.75–1.25
PDW	1,500–3,000	<50	1–3	34.5–34.7	>170	>2.5	<0.5
UCDW	200–2,000	>50	1–3	34.5–34.7	150–175	2.25–2.5	0.6–0.8
LCDW	200–4,000	>50	0–2	34.5–34.75	120–140	2–2.25	0.5–0.6
AABW	>4,000	>50	−2 to 1	34.7	100–120	2–2.2	0.5–0.6

Note. AOU = apparent oxygen utilization; STSW = Subtropical Surface Waters; SASW = subantarctic surface waters; LCDW = Lower Circumpolar Deep Water; SAMW = Subantarctic Mode Water; AAIW = Antarctic Intermediate Water; UCDW = Upper Circumpolar Deep Water; AABW = Antarctic Bottom Water.

2. Data and Methods

2.1. Hydrographic Data

Hydrographic, nutrient, carbon isotope ($\delta^{13}C_{DIC}$), and CFC data for the modern south Pacific were obtained from WOCE transects between 2000 and 2015 (P06, P16, and P18; Table 2 and Figure 1b; data available at https://ccdho.ucsd.edu/). In order to provide a map of the spatial variability in the $\delta^{13}C_{DIC}$, we used a multiple linear regression (MLR) approach, previously used by McNeil et al. (2001) and Eide, Olsen, Ninnemann, and Eldevik (2017), and Eide, Olsen, Ninnemann, & Johannessen, 2017, to estimate the modern $\delta^{13}C_{DIC}$ from the hydrographic parameters (potential temperature [θ], salinity, oxygen [apparent oxygen utilization, AOU], and density [σ_θ]). This produced a MLR equation (equation (1))

$$\delta^{13}C_{DIC} = 8.03 - (0.00483^{*}AOU) + (0.102^{*}\theta) + (0.561^{*}\sigma_\theta) - (0.651^{*}Salinity) \quad (1)$$

The MLR equation provides a good estimate of the $\delta^{13}C_{DIC}$ throughout the water column with a $R^2 = 0.93$ (Figure 3a). The residuals of the measured $\delta^{13}C_{DIC}$-estimated $\delta^{13}C_{DIC}$ from the MLR are shown in Figures 3b and 3c. The root-mean-square error for this data set is 0.11, and the standard deviation is 0.48. Other previous MLR efforts to determine the $\delta^{13}C_{DIC}$ have used additional parameters such as alkalinity (McNeil et al., 2001) and phosphate (Eide, Olsen, Ninnemann, Eldevik, 2017; Eide, Olsen, Ninnemann, & Johannessen, 2017). We found that the addition of phosphate into the MLR model showed no improvement in the results, especially north of the STF (Maxson, 2017), and there are few surface water alkalinity measurements (or good interpolations) for this region to use this parameter for a spatial surface distribution. The $\delta^{13}C_{DIC}$ estimated using this MLR was compared to independent measured $\delta^{13}C_{DIC}$ data from a transect south of New Zealand during voyage TAN1302 (Bass et al., 2014; supporting information Table S1). We also applied the same MLR approach on WOCE transects from the 1990s to determine the $\delta^{13}C_{DIC}$ for the southwest Pacific for the period 1990–2000 (see supporting information Table S2).

We used the MLR equation (1) to produce a spatial map of the estimated $\delta^{13}C_{DIC}$ for the surface waters of the southwest Pacific for Austral spring (October–December, the season when *G. bulloides* dominates sediment traps in the STSW and SASW [the latter also exhibits a second peak in summer] King & Howard, 2001) with a resolution of 1° × 1° using hydrographic data from the World Ocean Atlas (2013; Figure 4a). To determine the main processes driving the $\delta^{13}C_{DIC}$ in the surface waters of the ocean, we estimate the $\delta^{13}C$ from air-sea gas exchange of CO_2 using the equation originally derived by Kroopnick (1985) and revised by Keir et al. (1998)

Table 2
The 2000–2015 Voyages That Collected $\delta^{13}C_{DIC}$ Data

Transect	Dates	Ship	Principal scientist
P06	03/08/2003 to 16/10/2003	RV Mirai	S Watanabe/M Fukusawa
P06	21/11/2009 to 10/02/2010	RV Melville	A MacDonald, R Curry
P16	09/01/2005 to 19/02/2005	RV Revelle	B Sloyan, J Swift
P16	20/03/2014 to 05/05/2014	RV Nathaniel B Palmer	L Talley
P18	15/12/2007 to 23/2/2008	RV Ronald H Brown	J Bullister

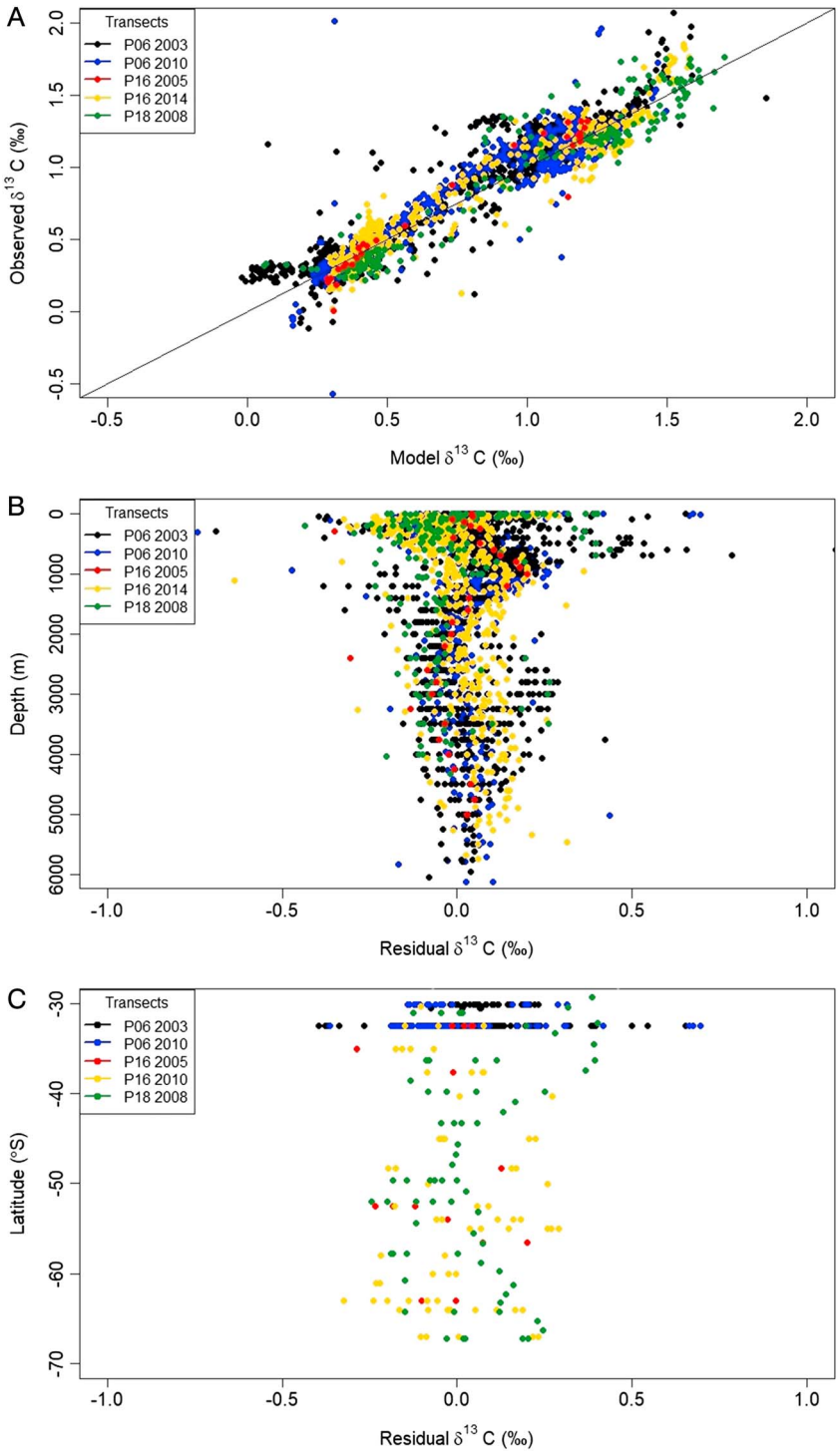

Figure 3. (a) Multiple linear regression residuals (model estimate vs. measured) black line is 1:1, (b) shows residuals with water depth (m), and (c) surface water (<200 m) residuals with latitude.

$$\delta^{13}C_{air-sea} = \delta^{13}C_{DIC} - (1.6 - 0.0074^{*}AOU)$$

where the $\delta^{13}C_{DIC}$ is estimated from the above MLR equation, the global correlation of $\delta^{13}C_{DIC}$ versus AOU has a slope of $0.0074‰ \cdot \mu mol^{-1} \cdot O_2 \cdot kg^{-1}$ and where 1.6‰ is the intercept for oxygen saturation. The $\delta^{13}C_{bio}$

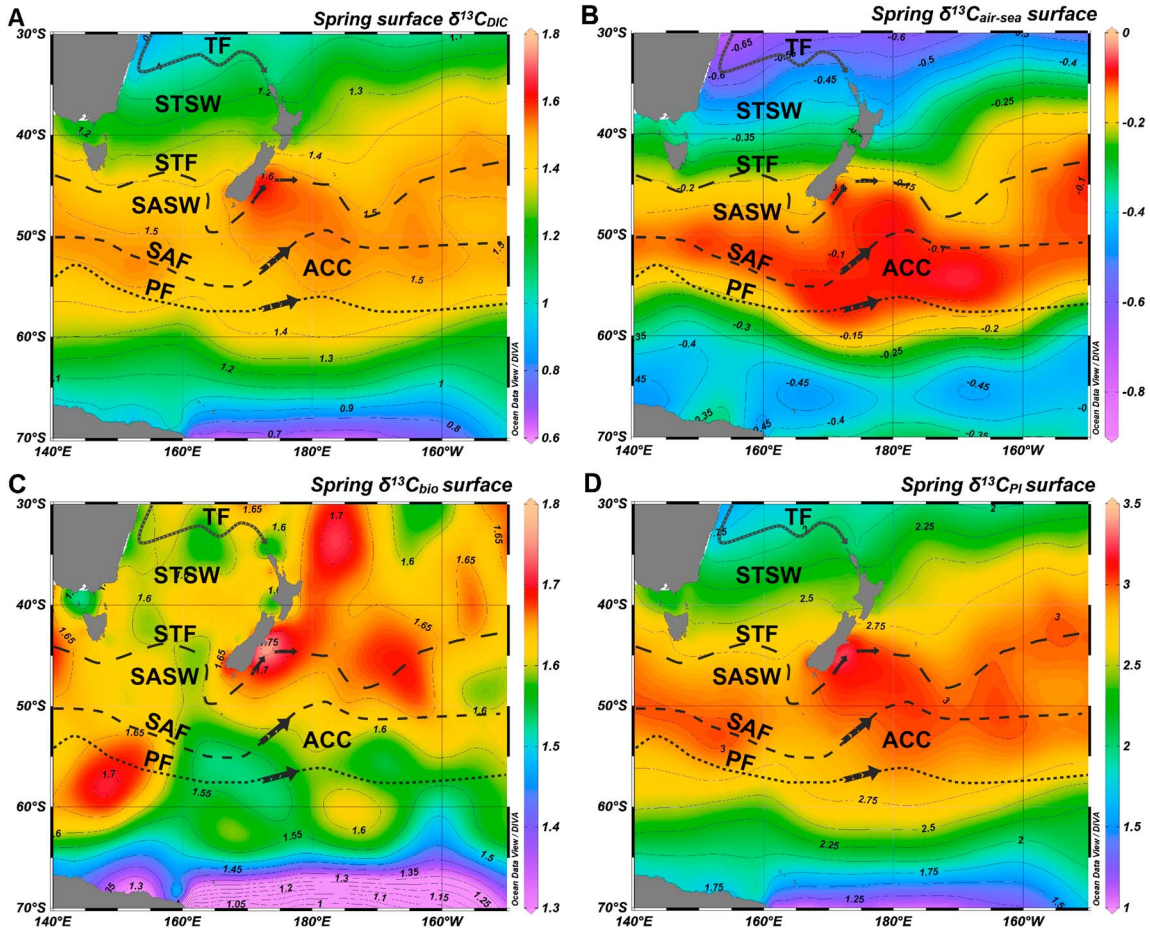

Figure 4. (a) Estimates of surface $\delta^{13}C_{DIC}$ during the 2000s based on the multiple linear regression (equation (1)) using the hydrographic data from the World Ocean Atlas (2013). (b) Estimates of the $\delta^{13}C_{air\text{-}sea}$. (c) Estimates of the $\delta^{13}C_{bio}$. (d) Estimates of the $\delta^{13}C_{PI}$ using the CFC two-step back calculation of Olsen and Ninnemann (2010) and Eide, Olsen, Ninnemann, & Eldevik, (2017), and Eide, Olsen, Ninnemann, and Johannessen (2017). Figure made with ODV (Schlitzer, 2009). Position of the fronts and currents adapted from Chiswell et al. (2015).

influences can then be determined from the $\delta^{13}C_{DIC}$-$\delta^{13}C_{as}$ (Gruber et al., 1999). The $\delta^{13}C_{air\text{-}sea}$ and $\delta^{13}C_{bio}$ for Austral spring are presented in Figures 4b and 4c.

To create our preindustrial (PI) model of the $\delta^{13}C_{PI}$ for the southwest Pacific, we used the two-step back-calculation procedure developed by Olsen and Ninnemann (2010). This process utilizes dissolved chlorofluorocarbon-11 (CFC-11) and $\delta^{13}C_{DIC}$ values measured on the WOCE transects P06 (2009), P16 (2005), and P18 (2007; Table 2) to quantify the relationship between the calculated values of preformed $\delta^{13}C$ and CFC-11 partial pressure in the atmosphere (pCFC-11). The second stage removes the anthropogenic signal from the modern $\delta^{13}C_{DIC}$ data. Details of this technique are described in Olsen and Ninnemann (2010), Eide, Olsen, Ninnemann, and Eldevik (2017), and Eide, Olsen, Ninnemann, & Johannessen (2017). The calculated $\delta^{13}C_{PI}$ for this region is shown in Figure 4d.

2.2. Sediment Core Data

We compiled published and unpublished carbon isotopes of *G. bulloides* ($\delta^{13}C_{G.bulloides}$) data from core tops ($n = 68$) and cores ($n = 19$) north, east, and south of New Zealand region over a latitudinal range of 34–57°S (Tables 3 and 4). The core tops do not have radiocarbon dates, and we assume that they are late Holocene (similar to a recent assessment of core tops east of New Zealand from Prebble et al., 2013). By using a large number of core top $\delta^{13}C_{G.bulloidesTC}$ data, major outliers should not significantly influence the final average Holocene latitudinal $\delta^{13}C_{G.bulloidesTC}$ transect. The core top $\delta^{13}C_{G.bulloidesTC}$ are also compared to the $\delta^{13}C_{PI}$ and the $\delta^{13}C_{DIC}$ from the 1970s, 1990s, and 2000s. Cores were chosen that had relatively high resolution

Table 3
Core Tops

Core	Latitude	Longitude	δ^{13}C *Globigerina bulloides*	Region	Mean Ann SST (°C)[a]	Reference
P71	−33.855	174.693	−1.03		19.31	Duncan et al. (2016)
S804	−35.853	177.285	−1.16	BoP	18.33	Wright et al. (1995)
RR0503-125JPC	−36.198	176.889	−1.27	BoP	18.27	Schiraldi et al. (2014)
S794	−36.310	177.997	−0.24	BoP	18.22	Wright et al. (1995) and Weaver et al. (1998)
H214	−36.925	177.442	−1.00	BoP	18.11	Samson et al. (2005)
H211	−37.303	177.358	−0.59	BoP	17.96	Neil (1997)
RR0503-64JPC	−37.422	177.002	−1.22	BoP	17.95	Schiraldi et al. (2014)
CHAT10K	−40.033	−179.996	−0.36	NCR	16.32	Weaver et al. (1998)
S938	−40.033	−179.996	−0.99	NCR	16.32	Neil (1997)
MD97-2121	−40.382	177.995	−1.10	NCR	16.23	Carter et al. (2008)
P69	−40.397	178.000	−0.63	NCR	16.23	Neil (1997)
S924	−41.583	−171.500	−0.37	NCR	14.86	Neil (1997)
ODP site 1123	−41.786	−171.499	−0.13	NCR	14.86	McCave et al. (2008) and this study
W266	−42.224	179.360	−0.61	NCR	15.10	Neil (1997)
R657	−42.533	−178.493	−0.54	NCR	14.41	Neil (1997)
U951	−42.715	176.913	0.09	NCR	14.29	Neil (1997)
W268	−42.851	178.969	0.08	NCR	14.04	Neil (1997)
Q213	−44.013	178.003	2.19	SCR	11.94	Neil (1997)
Q220	−44.292	174.975	0.15	SCR	12.04	Neil (1997)
U939	−44.494	179.501	0.62	SCR	11.77	Neil (1997)
H347	−44.532	173.417	−0.05	SCR	11.31	Neil (1997)
W272	−44.687	179.072	0.30	SCR	11.62	Neil (1997)
Q216	−45.025	177.057	−0.02	SCR	10.99	Neil (1997)
U938	−45.075	179.499	0.63	SCR	11.27	Weaver et al. (1998)
Q215	−45.387	177.993	0.48	SCR	11.01	Neil (1997)
DSDP 594	−45.524	174.948	0.44	SCR	10.61	Nelson et al. (1993)
Q203	−45.962	175.060	0.05	SCR	10.46	Neil (1997)
Q208	−45.987	177.988	0.23	SCR	10.86	Neil (1997)
Q200	−45.995	172.025	0.31	SCR	10.32	Weaver et al. (1998)
Q217	−46.465	175.067	−0.19	SCR	10.31	Neil (1997)
A825	−46.587	167.500	0.01	SolN	12.31	This study
Q582	−46.597	−177.917	−0.05	SCR	10.98	Neil (1997)
A830	−46.708	167.083	−0.01	SolN	12.45	This study
C887	−46.750	165.875	0.03	SolN	12.49	This study
TAN1106-7	−46.770	166.920	−0.31	SolN	12.49	This study
A831	−46.840	167.072	−0.56	SolN	12.49	This study
A832	−46.970	167.075	−0.12	SolN	12.49	This study
E824	−46.975	166.547	−0.67	SolN	12.33	This study
TAN0803-09	−46.997	166.061	−0.32	SolN	12.25	This study
V16-121	−47.000	172.000	0.43		9.92	Ninnemann and Charles (1997)
H564	−47.043	174.078	−0.01		10.06	Neil (1997)
A833	−47.083	167.083	0.08	SolN	12.33	This study
A845	−47.092	166.800	−0.14	SolN	12.36	This study
TAN1106-11	−47.165	166.649	0.15	SolN	12.32	This study
A846	−47.320	166.575	−0.06	SolN	12.16	This study
TAN1106-15	−47.389	166.013	−0.21	SolN	12.06	This study
A847	−47.450	166.783	−0.39	SolN	11.97	This study
TAN1106-89	−47.971	169.360	0.32		10.09	This study
TAN1106-28	−48.372	165.659	1.04	SolN	11.12	This study
MD97-2110	−48.430	176.570	0.51		8.77	King and Howard (2004)
F104	−48.667	170.808	0.58		9.66	Neil (1997)
TAN0803-24	−48.797	165.296	0.28	SolN	10.63	This study
F111	−48.950	174.975	0.53		8.70	Neil (1997)
TAN1106-34	−49.302	165.166	0.01	SolN	10.16	This study
TAN0803-27	−49.524	164.609	0.93	SolN	10.03	This study
Q585	−49.670	−177.990	0.57	SolS	8.88	Weaver et al. (1997)
D84	−49.775	168.933	0.06	SolS	9.42	Neil (1997)
ODP site 1120	−50.063	173.372	0.30		8.91	Neil et al. (2004)
TAN0803-40	−50.432	164.287	−0.07	SolS	9.37	This study
TAN1106-43	−50.449	164.878	0.86	SolS	9.40	This study

Table 3 *(continued)*

Core	Latitude	Longitude	$\delta^{13}C$ *Globigerina bulloides*	Region	Mean Ann SST (°C)[a]	Reference
F149	−50.517	174.317	0.25		8.38	Neil (1997)
D206	−50.600	171.392	−0.05		8.96	Neil (1997)
Q589	−50.785	176.772	−0.69		7.64	Neil (1997)
D169	−50.792	163.958	0.20	SolS	9.20	This study
V16-122	−51.000	164.000	0.51	SolS	9.05	Ninnemann and Charles (1997)
TAN1106-47	−51.266	165.040	−0.12	SolS	9.10	This study
E236	−54.995	158.607	0.60		5.29	This study
TAN1302-97	−57.286	161.331	0.68		2.95	This study

Note. BoP = Bay of Plenty; NCR = North Chatham Rise; SCR = South Chatham Rise; SolN = Northern Solander Trough; SolS = Southern Solander Trough.
[a]WOA2013 Mean Annual SST.

(with sample resolution of <1 kyr) for the last 25 kyr. Carbon isotopes have been found to vary with test size in *G. bulloides* (Birch et al., 2013; Elderfield et al., 2002). The majority of the stable isotopes were run on *G. bulloides* tests from the 250- to 355-μm size fraction for the TAN cores, JP cores, and the MD97-2120 (Bostock et al., 2015; Pahnke et al., 2003; Schiraldi et al., 2014); however, different size ranges were used for a couple of the cores: H214 used 180–300 μm (Samson et al., 2005); ODP 1123 and CHAT10K cores were run using 300–355 μm and for MD97-2121 the >150-μm size range (Carter et al., 2008). The core tops and cores were grouped into five different regions (Figure 1a and Tables 3 and 4). These include the Bay of Plenty (BOP), influenced by warm STSW, the North Chatham Rise (NCR) influenced by STSW/STF, South Chatham Rise (SCR) influenced by STF/SASW, Northern Solander Trough (SolN) influenced by the STF, and the Southern Solander Trough (SolS) STF/SASW (Figure 1a).

We used the previously developed chronology for all the published cores in this study (Table 3). For the cores that did not have age models (TAN1106-07, TAN1106-11, and TAN0803-27) two methods were used: comparing the $\delta^{18}O$ *G. bulloides* record from the core with a global benthic $\delta^{18}O$ stack record (e.g., LR04; Lisiecki & Raymo, 2005) and calibrated radiocarbon ages to provide additional tie points for the $\delta^{18}O$ age model. Radiocarbon data were corrected for the reservoir ages of the core location using an estimate from the global models (Butzin et al., 2005) and final calibrated ages obtained using Calib 7.1 and the MARINE13 calibration curve (Reimer et al., 2013). Age data and radiocarbon dates are provided for these three cores in the supporting information Table S3.

King and Howard (2004) determined that the difference between $\delta^{13}C_{G.bulloides}$ values and $\delta^{13}C_{DIC}$ values from sediment trap samples in the southwest Pacific region is primarily dependent on the temperature of the water in which they are formed, in agreement with the experimental disequilibrium from ambient seawater equation ($\delta^{13}C_{G.bulloides} - \delta^{13}C_{DIC} = (-0.11*T)-0.77$) determined by Bemis et al. (2000) for oceanic temperatures (0–25 °C). We used this equation to correct the $\delta^{13}C_{G.bulloides}$ data to equivalent $\delta^{13}C_{DIC}$ values ($\delta^{13}C_{G.bulloidesTC}$) to allow us to compare $\delta^{13}C_{DIC}$ equivalent data between regions over time. Based on the $\delta^{18}O$, *G. bulloides* lives in the top 100 m of the ocean around New Zealand, within the upper mixed layer (Maxson, 2017). Therefore, we used mean Annual sea surface temperatures (SST) from the World Ocean Atlas (2013; Table 3), which is similar to the Spring SST when the *G. bulloides* is dominant (King & Howard, 2001), to calculate the $\delta^{13}C_{G.bulloidesTC.}$ This is also consistent with the downcore records where we used the annual mean SST estimates from proxy records where the core top SST values agree with the modern annual mean SST measurements. Unfortunately, for many of the cores paleo-SST estimates were not available and we have had to use SST estimates from cores in the same region or same water mass (Table 4). For example we used the alkenone SST estimates from the STW influenced NCR (Pahnke & Sachs, 2006) to correct the $\delta^{13}C_{G.bulloides}$ data from the BOP as the SST estimates from foraminiferal assemblages from core H214 do not extend back beyond 16 ka (Samson et al., 2005). The use of paleo-SST estimates from other cores (and sometimes in different regions) to correct the $\delta^{13}C_{G.bulloides}$ is not ideal; the relative changes in SST in the different water masses between the glacial and Holocene provide suitable corrections to look at the large-scale changes in $\delta^{13}C_{G.bulloidesTC}$ across the southwest Pacific over the last 25 kyr.

Table 4
Core Data

Zone	Core	Latitude	Longitude	Depth (m)	$\delta^{13}C_{G.bulloides}$ reference	Reference for core	SST reconstructions used
BoP	RR0503-125JPC	−36.198	176.889	2541	Schiraldi et al. (2014)	Schiraldi et al. (2014)	MD97-2121 Alkenone SST, Pahnke and Zahn (2005)
	H214	−36.925	177.442	2045	This study	Samson et al. (2005)	MD97-2121 Alkenone SST, Pahnke and Zahn (2005)
	RR0503-79JPC	−36.959	176.593	1165	Schiraldi et al. (2014)	Schiraldi et al. (2014)	MD97-2121 Alkenone SST, Pahnke and Zahn (2005)
	RR0503-87JPC	−37.264	176.664	663	Schiraldi et al. (2014)	Schiraldi et al. (2014)	MD97-2121 Alkenone SST, Pahnke and Zahn (2005)
	RR0503-64JPC	−37.422	177.002	651	Schiraldi et al. (2014)	Schiraldi et al. (2014)	MD97-2121 Alkenone SST, Pahnke and Zahn (2005)
NCR	CHAT10K	−40.033	−179.996	3003	This study	McCave et al. (2008)	MD97-2121 Alkenone SST, Pahnke and Zahn (2005)
	MD97-2121	−40.382	177.995	2314	Carter et al. (2008)	Carter et al. (2008)	MD97-2121 Alkenone SST, Pahnke and Zahn (2005)
	ODP site 1123	−41.786	−171.499	3290	This study	McCave et al. (2008)	MD97-2121 Alkenone SST, Pahnke and Zahn (2005)
SCR	ODP site 1119	−44.756	172.393	396	Carter and Gammon (2004)	Carter and Gammon (2004)	MD97-2120 Alkenone SST, Pahnke and Zahn (2005)
	DSDP 594	−45.524	174.948	1204	Nelson et al. (1993)	Nelson et al. (1993)	MD97-2120 Alkenone SST, Pahnke and Zahn (2005)
	MD97-2120	−45.534	174.931	1210	Schiraldi et al. (2014)	Pahnke et al. (2003)	MD97-2120 Alkenone SST, Pahnke & Zahn(2005)
SolN	TAN1106-7	−46.77	166.92	743	This study	This study	TAN0803-9 Foram MAT SST, Bostock et al. (2015)
	TAN0803-9	−46.997	166.061	1648	This study	Bostock et al. (2015)	TAN0803-9 Foram MAT SST, Bostock et al. (2015)
	TAN1106-11	−47.165	166.649	1349	This study	This study	TAN0803-9 Foram MAT SST, Bostock et al. (2015)
	TAN1106-15	−47.389	166.013	2544	This study	This study	TAN0803-9 Foram MAT SST, Bostock et al. (2015)
	TAN1106-28	−48.372	165.659	2798	This study	Bostock et al. (2015)	TAN0803-9 Foram MAT SST, Bostock et al. (2015)
SolS	TAN1106-34	−49.302	165.166	3416	This study	Bostock et al. (2015)	TAN1106-43 Foram MAT SST, Bostock et al. (2015)
	TAN0803-27	−50.432	164.287	3524	This study	This study	TAN1106-43 Foram MAT SST, Bostock et al. (2015)
	TAN1106-43	−50.449	164.878	3670	This study	Bostock et al. (2015)	TAN1106-43 Foram MAT SST, Bostock et al. (2015)

Note. SST = sea surface temperature.

Culture experiments have suggested that $\delta^{13}C_{G.bulloides}$ is also dependent on the dietary carbon composition ($\delta^{13}C_{org}$; 0.084‰/1‰ change in organic carbon; Spero & Lea, 1996) and the concentration of the carbonate ion, ($-0.012‰\cdot[CO_3^{2-}]$ $\mu mol^{-1}\cdot kg^{-1}$; Spero et al., 1997). Unfortunately, there is no data on past changes in either the organic carbon stable isotope values or the carbonate ion concentration over the last 25 kyr, and therefore, we have not undertaken these corrections. The King and Howard (2004) study measured $\delta^{13}C_{G.bulloides}$ from a series of modern sediment traps from 42.5°S to 54°S in the southwest Pacific, covering a wide range of carbonate ion concentrations and $\delta^{13}C_{org}$ and found that the vital effects were primarily removed by the temperature correction. Thus, temperature, which affects these factors, may offset or compensate for them. Alternatively, the influences from the carbonate ion and organic $\delta^{13}C$ cancel each other out.

Planktic $\delta^{13}C$ are typically noisy and hard to interpret. To determine the main long-term trends in the $\delta^{13}C_{DIC}$ equivalent data for each region, we combined downcore $\delta^{13}C_{G.bulloidesTC}$ data sets from the same region (e.g., BoP and NCR) using a Monte Carlo simulation in the program R, which considers the analytical and chronological errors to provide a statistically robust long-term trend (Khider et al., 2017). For the analytical error for $\delta^{13}C_{G.bulloides}$ we used ±0.05‰ and all $\delta^{13}C$ are reported with respect to the Vienna Peedee Belemite (vpdb) standard (Carter et al., 2008; Schiraldi et al., 2014). Our age model error was estimated to be ±250 years (based on the radiocarbon errors and allowing for uncertainty in the radiocarbon reservoir age; ±500 years and ±1,000 years were also tested and made little difference to the results, apart from increased smoothing). All Monte Carlo simulations were run through 1,000 iterations. The standard deviation of the Monte Carlo data was calculated (Table 5 and Figure 6). In order to compare the latitudinal gradients in $\delta^{13}C$ over the last 25 kyr, the average $\delta^{13}C_{G.bulloidesTC}$ Monte Carlo simulation for each region was plotted against latitude for seven different 2-kyr time slices: Glacial (24–22 ka), Last Glacial Maximum (LGM; 20–18 ka), early deglaciation (18–16 ka), Antarctic cold reversal (ACR; 15–13 ka), early Holocene (12–10 ka), mid-Holocene (8–6 ka), and late Holocene (4–2 ka).

3. Results

3.1. Modern and PI $\delta^{13}C$ in the Southwest Pacific

The strong relationship between the $\delta^{13}C_{DIC}$ estimated from the MLR using hydrographic data and the measured $\delta^{13}C_{DIC}$ (Figure 3a) suggests that this is a robust approach to determine the spatial distribution of the $\delta^{13}C_{DIC}$ in regions like the southwest Pacific that is undersampled for this parameter (Figure 2e). The highest residual errors (up to ±0.2‰) between the measured and the estimated are in the surface waters (Figure 3b). The highest errors are in the lower-latitude surface waters (Figure 3c), but this is likely due to the fact that there is more data at this latitude (P06, 30–32°S; Figure 1b). The subsurface residuals are slightly lower (±0.15‰; Figure 3b). This suggests that the seasonal variability and the biological productivity in the surface waters are not completely captured by the hydrographic data. This is evident when the MLR was tested on an independent $\delta^{13}C_{DIC}$ data set from a voyage transect (TAN1302) south of New Zealand to Antarctica (Bass et al., 2014, and

Table 5
Standard Deviations of the Monte Carlo Simulations for the $\delta^{13}C_{G.bulloides}$ Data From Each Region

Time interval	BoP	NCR	SCR	SolN	SolS
Late Holocene (8–0 ka)	0.287	0.567	0.253	0.337	0.353
Early Holocene (12–8 ka)	0.302	0.533	0.246	0.197	0.358
Antarctic cold reversal (15–13 ka)	0.297	0.578	0.212	0.196	0.394
Early deglaciation (18–14 ka)	0.274	0.548	0.386	0.387	0.287
Last glacial maximum (21–18 ka)	0.55	0.662	0.573	0.324	0.355
Glacial (25–21 ka)	0.242	0.431	0.427	0.376	0.501

Note. BOP = Bay of Plenty; NCR = North Chatham Rise; SCR = South Chatham Rise; SolN = Northern Solander Trough; SolS = Southern Solander Trough.

supporting information Table S1). The $\delta^{13}C_{DIC}$ estimated from the MLR is in good agreement with the measured data for the majority of the TAN1302 New Zealand to Antarctic transect, but there are two regions in the north near the STF (45–47°S), and south on the Antarctic continental shelf (63–65°S), where the measured $\delta^{13}C_{DIC}$ data are higher than estimated.

We used the MLR equation to produce a map of surface $\delta^{13}C_{DIC}$ distributions for Austral spring for the southwest Pacific (Figure 4a). The $\delta^{13}C_{DIC}$ map shows the highest $\delta^{13}C_{DIC}$ between 42–60°S. North of 42°S and south of 60°S the $\delta^{13}C_{DIC}$ declines from values of 1.4 to 1‰. The highest $\delta^{13}C_{air\text{-}sea}$ values (−0.15‰ to 0‰) are also evident between 42–60°S (Figure 4b). The lowest $\delta^{13}C_{air\text{-}sea}$ values (−0.65‰ to −0.3‰) are north of 42°S, while south of 60°S the values are also low (−0.45‰ to −0.3‰). The $\delta^{13}C_{bio}$ is more heterogeneous (Figure 4c). The highest $\delta^{13}C_{bio}$ values (1.65–1.75‰) are along the STF (~45°S), with some additional highs in the STSW east of New Zealand (53–60°S; 180–170°W) and south of Tasmania (55–60°S, 140–155°E). South of 60°S the $\delta^{13}C_{bio}$ values are <1.6‰.

The 2000s $\delta^{13}C_{DIC}$ values are mostly lower than the $\delta^{13}C_{DIC}$ values estimated for the 1990s (Figure 5b), although the 1990s data show similar spatial patterns (supporting information Table S2). The largest difference between the estimated 1990s and 2000s $\delta^{13}C_{DIC}$ along 180° is ~0.4‰ in the STSW (30–43°S; Figure 5b); this declines to ~0.2‰ at 45°S, while the $\delta^{13}C_{DIC}$ values for the 1990s and 2000s are similar south of 50°S.

The estimated $\delta^{13}C_{PI}$ values for the surface waters display a greater range than the modern $\delta^{13}C_{DIC}$ values (Figures 4d and 5b). The estimated surface water $\delta^{13}C_{PI}$ along the longitudinal 180° transect (Figure 5b) show a low $\delta^{13}C_{PI}$ of 2‰ at 30°S, increasing steadily to 2.5‰ at 40°S. The $\delta^{13}C_{PI}$ values rapidly increase between 40°S and 45°S to peak values of >3‰ and then a slow and steady decline from 50°S to values of ~2.75‰ at 60°S. The CFC method for calculating $\delta^{13}C_{PI}$ is more suitable for water depths deeper than 200 m (Olsen & Ninnemann, 2010); thus, we calculated $\delta^{13}C_{PI}$ for 200-m water depth along 180° (Figure 5b). Between 30°S and 40°S the $\delta^{13}C_{PI}$ values at 200 m are similar to the surface $\delta^{13}C_{PI}$ and then display a steady rise to peak values of ~2.75‰ at 55°S and then decrease to <2.5‰ by 60°S. The primary differences between the surface $\delta^{13}C_{PI}$ and those at 200-m water depth are due to a shallower mixed layer and thermocline at higher latitudes. South of 60–65°S, there is a steep latitudinal gradient in $\delta^{13}C_{PI}$ (Figure 4d).

3.2. Core Top $\delta^{13}C_{G.bulloides}$

Core top $\delta^{13}C_{G.bulloides}$ values range from −1‰ to 1‰ (Table 3 and Figure 5a). The $\delta^{13}C_{G.bulloides}$ values generally increase with latitude, with some minor fluctuations between 40°S and 50°S (Figure 5a). Core top temperature corrected $\delta^{13}C_{G.bulloidesTC}$ values have a larger range from about 1‰ to 2.8‰ (Figure 5a). There is a general trend of high average $\delta^{13}C_{G.bulloidesTC}$ values in the north between 30°S and 43°S (2–2.25‰) and low average values in the south between 50°S and 60°S (1.5–1.75‰). In between there are two peaks in $\delta^{13}C_{G.bulloidesTC}$ near ~50°S and ~45°S.

In the north (30–40°S) these $\delta^{13}C_{G.bulloidesTC}$ values are similar to the $\delta^{13}C_{PI}$, while in the midlatitudes the majority of the $\delta^{13}C_{G.bulloidesTC}$ values (taking into account the analytical error using the Monte Carlo simulation) sit within the envelope between the surface $\delta^{13}C_{PI}$ and modern $\delta^{13}C_{DIC}$ modern. The exception is south between 50°S and 60°S, where the $\delta^{13}C_{G.bulloidesTC}$ are well below the $\delta^{13}C_{PI}$ (both surface, 100 and

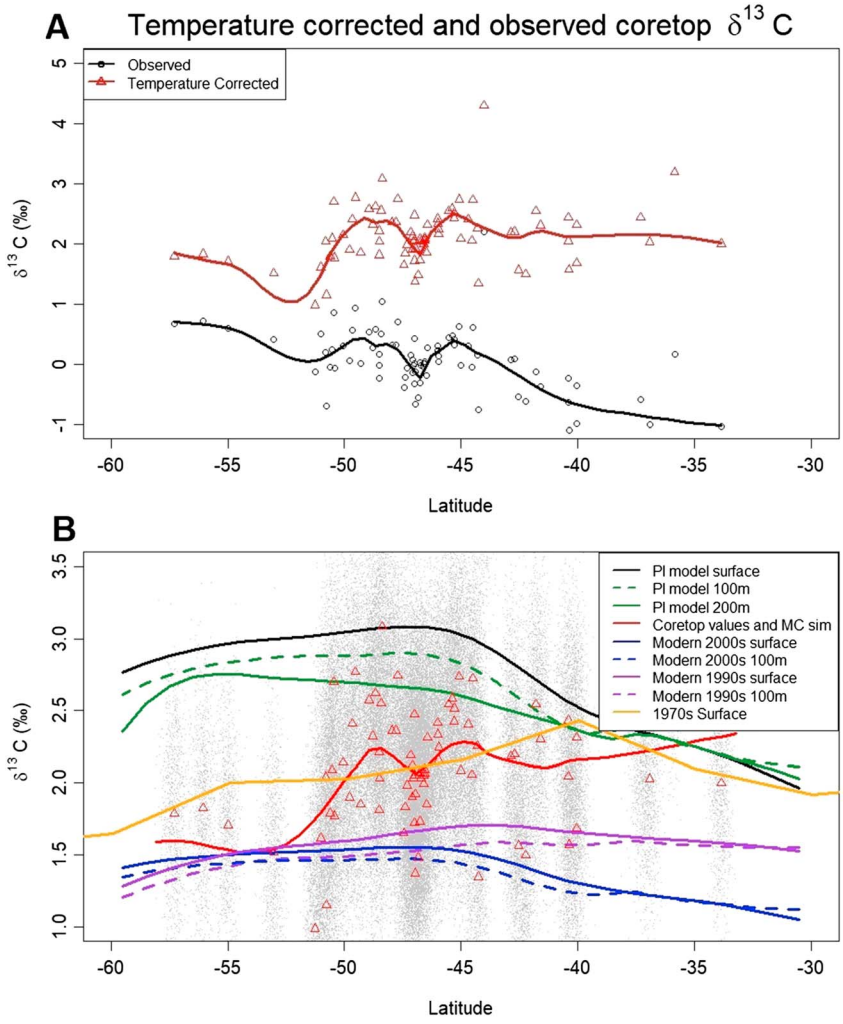

Figure 5. (a) The $\delta^{13}C_{G.bulloides}$ data from the core tops (Table 3) against latitude. Raw data $\delta^{13}C_{G.bulloides}$ (black circles and line), $\delta^{13}C_{G.bulloidesTC}$ values (red triangles and line). (b) Modern 2000s $\delta^{13}C_{DIC}$ for spring (surface (0 m) = blue line, 100 m = blue dashed line) calculated from multiple linear regression algorithm along 180° longitude (Figure 1b), modern 1990s $\delta^{13}C_{DIC}$ for spring (surface = purple line, 100 m = purple dashed line) calculated along 180° longitude (supporting information Table S2), surface $\delta^{13}C_{PI}$ (surface = black line, 100 m = green dashed line, 200 m = green line) along 180°longitude. The 1970s Hudson $\delta^{13}C_{DIC}$ (surface = yellow line) data for 150°W are in yellow (Lynch-Stieglitz et al., 1995; Quay et al., 1992). Core top $\delta^{13}C_{G.bulloidesTC}$ (red triangles and average = red line) and the Monte Carlo simulation (gray dots). The $\delta^{13}C_{DIC}$ for 100-m depth is displayed as *Globigerina bulloides* live in the upper 100 m of the water column. BOP = Bay of Plenty; NCR = North Chatham Rise; SCR = South Chatham Rise.

200 m) values, and the mean $\delta^{13}C_{G.bulloidesTC}$ Monte Carlo values is between the modern $\delta^{13}C_{DIC}$ ranges for (both the 1990s and 2000s).

3.3. Sediment Core $\delta^{13}C_{G.bulloides}$ for Each Region

3.3.1. BOP

Five cores were used in this region. The $\delta^{13}C_{G.bulloides}$ of four of these cores (JPC 64, 79, 87, and 125) were previously published by Schiraldi et al. (2014), while the $\delta^{13}C_{G.bulloides}$ data from (H214) were not previously published for this core (Samson et al., 2005). The $\delta^{13}C_{G.bulloides}$ trends from the five cores are relatively similar (Figure 6a) but have a large spread of $\delta^{13}C_{G.bulloides}$ values (approximately 1‰) during the LGM. The Monte Carlo average temperature corrected $\delta^{13}C_{G.bulloidesTC}$ values are significantly higher than the uncorrected $\delta^{13}C_{G.bulloides}$, varying from 1.2‰ to 2.2‰ (Figure 6b). The trend obtained from the Monte Carlo simulation has stable $\delta^{13}C$ levels in the glacial (21–25 ka) at 1.75–2‰ (Figure 6b). At 20 ka there is a major drop in $\delta^{13}C$ by 0.75‰ to the lowest values of ~1.3‰ at 18 ka, during the LGM (defined here as 21–18 ka). However,

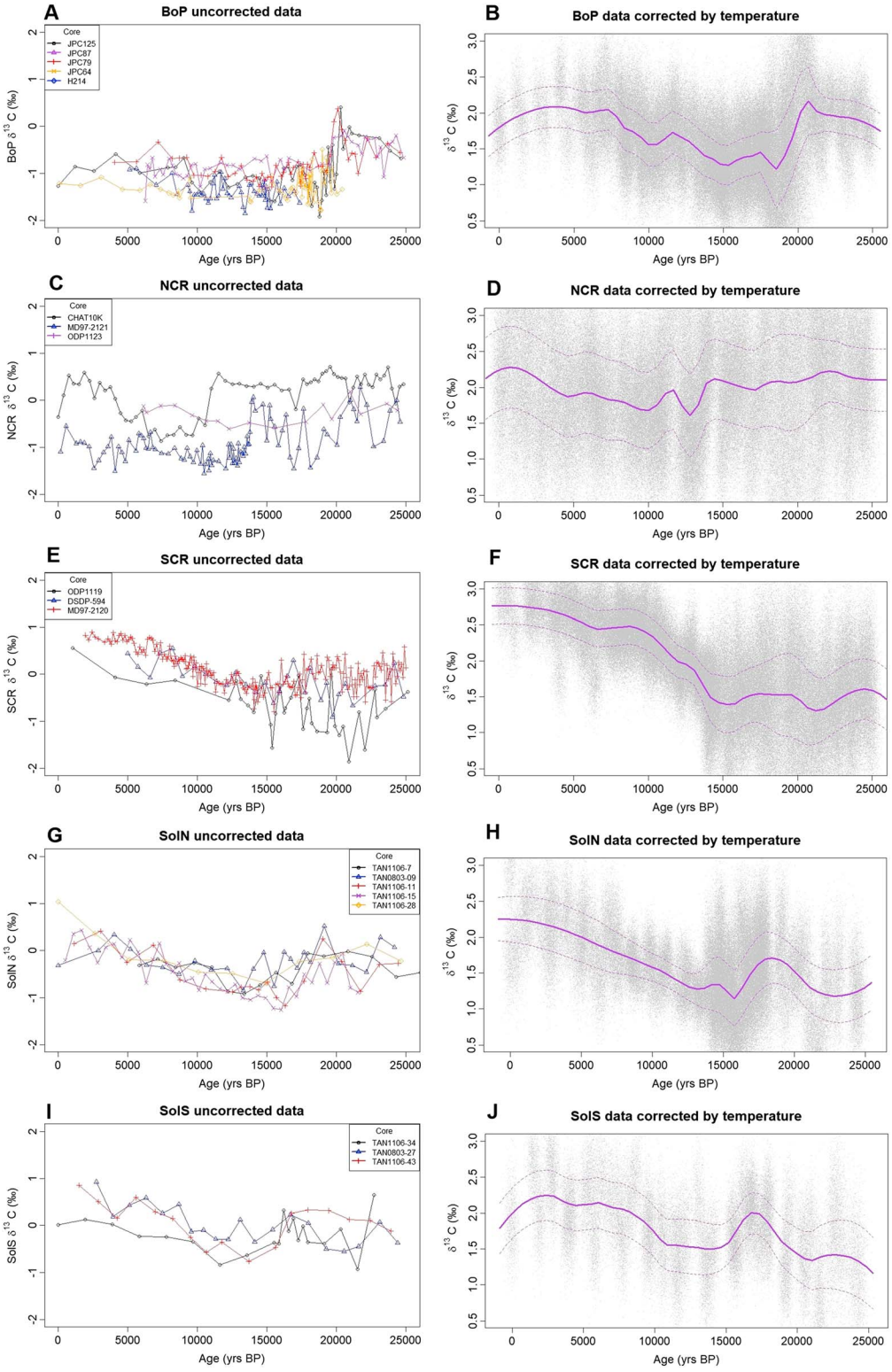

Figure 6. The $\delta^{13}C_{G.bulloides}$. Uncorrected downcore data (a, c, e, g, i) and temperature corrected $\delta^{13}C_{G.bulloides TC}$ Monte Carlo simulation with 1,000 iterations for the last 25 kyr for the five regions (b, d, f, h, j) using and error of ±250 years for the *s* axis and ±0.05‰ for the *y* axis. The purple line is the mean of the Monte Carlo simulation, and the purple dashed lines show the standard deviation. (a, b) Bay of Plenty (BOP), (c, d) North Chatham Rise (NCR), (e, f) South Chatham Rise (SCR), (g, h) Solander Trough North (SolN), and (i, j) Solander Trough South (SolS). See Table 4 for core information for each region.

during this time period the standard deviation of the $\delta^{13}C$ data is high (standard deviation, sd = 0.55; Table 5), indicating the least agreement between the cores. A steady increase in $\delta^{13}C_{G.bulloidesTC}$ is seen during the deglaciation to mid-Holocene from 18 to 7 ka (discounting two minor drops that are within the standard deviation of the data). During the late Holocene the values range between 1.75‰ and 2‰.

3.3.2. NCR

The NCR is made up of three cores: MD97-2121, ODP site 1123, and CHAT 10K (Table 4). MD97-2121 $\delta^{13}C_{G.bulloides}$ data (Carter et al., 2008) is by far the highest-resolution core of the three (Figure 6c) with values ranging from −1.5‰ to 0.3‰. ODP1123 generally follows the trend of MD97-2121 until approximately 14 ka, where higher $\delta^{13}C_{G.bulloides}$ values in ODP site 1123 are seen. The largest disagreement in $\delta^{13}C$ (~2‰) is between CHAT10K and MD97-2121 between 14 and 11 ka. These differences may be explained by the use of different size fractions used for the stable isotopes (300–355 μm for CHAT10K and ODP site 1123 versus >150 μm for MD97-2121), although this cannot account for the large differences between $\delta^{13}C_{G.bulloides}$ in CHAT10K and ODP site 1123. The Monte Carlo simulation of the $\delta^{13}C_{G.bulloidesTC}$ data gives a range of 1.75–2.75‰ (Figure 6d), but the large sd (043–0.66; Table 5) reflect the large intercore differences. The glacial and LGM $\delta^{13}C_{G.bulloidesTC.}$ Monte Carlo values are relatively stable (2–2.25‰). These stable values continue up to 17.5 ka. There is an increase to a maximum $\delta^{13}C_{G.bulloidesTC}$ value of 2.2‰ at 14.5 ka followed by another smaller peak at 12 ka of 2.0‰. The $\delta^{13}C_{G.bulloidesTC}$ values steadily climb from 11 to 8 ka where they level off at 2.0‰ until 4 ka then increase to 2.25‰ in the late Holocene (Figure 6d).

3.3.3. SCR

MD97-2120 has the highest values relative to the other cores in the region and is the least variable in its $\delta^{13}C_{G.bulloides}$ values (Figure 6e). DSDP 594 and ODP site 1119 are lower and more variable through time. Differences in $\delta^{13}C_{G.bulloides}$ values between the cores varies through time. The Monte Carlo simulation gives average $\delta^{13}C_{G.bulloidesTC}$ range from 1.3‰ to 2.75‰ (Figure 6f) and is dominated by the high-resolution MD97-2120 data set, since it contains >75% of the data for this zone (Figure 6e). Glacial, LGM, and early deglacial standard deviations are high (sd 0.43–0.57; Table 5). Low $\delta^{13}C_{G.bulloidesTC}$ values (1‰) persist from 25 to 15 ka. A rapid upward trend occurs between 15 and 9 ka with a slight decrease in rate between 14 and 12 ka. The $\delta^{13}C_{G.bulloidesTC}$ values level off from 9 to 6 ka at 2.5‰, increasing to 2.75‰ in the late Holocene. ACR and Holocene standard deviations are some of the lowest (sd 0.21–0.25; Table 5).

3.3.4. SolN

SolN contains five cores of relatively low resolution (TAN1106-7, 11, 15, 28; TAN0803-09) (Figure 6g). During the glacial and LGM the $\delta^{13}C_{G.bulloides}$ display a wide range in values (−0.8–0.5‰), the values decline in the early deglaciation. From 15 ka onward the $\delta^{13}C_{G.bulloides}$ show less range in values and a steady increase to the late Holocene. The Monte Carlo simulation gives average $\delta^{13}C_{G.bulloidesTC}$ range from 1.2‰ to 2.25‰ (Figure 6h). The standard deviations of the glacial, LGM, and early deglacial time slices suggest that there is more variability in these time slices (Table 5), compared to the later ACR and early Holocene. Glacial $\delta^{13}C_{G.bulloidesTC}$ levels are low at 1.25‰ (Figure 6h). At 22 ka a rise in $\delta^{13}C$ levels begins and continues until approximately 18 ka to a value of 1.75‰. This is followed by a sharp decline to values of 1.2‰ by 15 ka, followed by a rise in $\delta^{13}C_{G.bulloidesTC}$ values from ~14 to 2 ka to values of 2.25‰.

3.3.5. SolS

Three low-resolution cores are used for this zone (TAN1106-34, 43; TAN0803-27) (Figure 6i and Table 4). The cores display glacial and LGM $\delta^{13}C_{G.bulloides}$ values of −1‰ to 0.5‰; the values then decline during the deglaciation (−0.8‰ to 0.1‰), before steadily increasing during the Holocene. The Monte Carlo simulation gives average $\delta^{13}C_{G.bulloidesTC}$ values that range from 1.2‰ to 2.2‰ (Figure 6i). Standard deviations of this zone are higher than those of the SolN but still relatively good (sd <0.4, except for the glacial; Table 5). The average $\delta^{13}C_{G.bulloidesTC}$ is ~1.3‰ between 25 to 20 ka (Figure 6j). From 20 to 18 ka there is a rapid rise to a peak in $\delta^{13}C_{G.bulloidesTC}$ values of 2‰ at 17 ka; this is followed by a fall over the next 2 kyr to values of 1.5‰ between 15 and 10 ka. The $\delta^{13}C_{G.bulloidesTC}$ values rise again in the Holocene ranging from 1.75‰ to 2.2‰.

4. Discussion

4.1. Modern and Preindustrial $\delta^{13}C$ Spatial Distribution

The surface water estimated $\delta^{13}C_{DIC}$ from the MLR algorithm displays a distinct pattern, with peak values between 42°S and 60°S and low values to the north and south (Figure 4a). This is similar to measured

$\delta^{13}C_{DIC}$ patterns with a peak at ~45°S evident in previous transects across the South Pacific (150°W; Quay et al., 1992; Lynch-Stieglitz et al., 1995; Gruber et al., 1999). However, the high residuals (±0.2) of the estimated $\delta^{13}C_{DIC}$ in the surface waters suggest that the MLR is not capturing all the variability. A comparison of the $\delta^{13}C_{DIC}$ estimated from the MLR data with an independent surface water $\delta^{13}C_{DIC}$ data set, TAN1302 (Bass et al., 2014), shows good correlation between the data from the majority of this TAN1302 transect between New Zealand and Antarctica but some poor agreements between 45–47°S and 63–65°S (supporting information Table S1). These peaks in $\delta^{13}C_{DIC}$ on the TAN1302 transect are associated with regions of high productivity of the STF east of New Zealand and on the Antarctic continental shelf. The $\delta^{13}C_{bio}$ displays the highest values east of the South Island of New Zealand along the dynamic STF, where the TAN1302 transect traveled (Figure 4c; Bass et al., 2014). The $\delta^{13}C_{bio}$ is relatively high for the entire region north of the 60°S (Figure 4c), indicating that biological control has a strong influence on the $\delta^{13}C_{DIC}$. However, the estimated $\delta^{13}C_{DIC}$ spatial pattern in the southwest Pacific is more similar to the $\delta^{13}C_{air\text{-}sea}$ with a broad peak between 42°S and 60°S (Figures 4a and 4b). The $\delta^{13}C_{air\text{-}sea}$ is controlled by the SST and the residence times of the surface waters and the wind speeds (Broecker & Maier-Reimer, 1992; Gruber et al., 1999; Lynch-Stieglitz et al., 1995; Mook, 1986). In STSW the warm SST and long residence times of these surface waters result in a thermodynamic isotopic equilibration and lower $\delta^{13}C_{air\text{-}sea,}$ (Lynch-Stieglitz et al., 1995; Mook, 1986). South of the PF (~60°S), the $\delta^{13}C_{DIC}$ of the cold AASW is also low, but as the residence time of the water is too short for isotopic equilibration, this also results in low $\delta^{13}C_{air\text{-}sea}$ (Broecker & Maier-Reimer, 1992). The SASW are intermediate, with cool SST, and some equilibration, giving the highest $\delta^{13}C_{air\text{-}sea}$.

The estimated $\delta^{13}C_{DIC}$ for the surface waters of the southwest Pacific, along 180° longitude during the 2000s, are significantly lower than the estimated $\delta^{13}C_{DIC}$ values from the 1990s (Figure 5b and supporting information Table S2) and the 1970s (HUDSON70 voyage along 150°W; Figures 1a and 5b; Quay et al., 1992; Lynch-Stieglitz et al., 1995). In the 1970s the $\delta^{13}C_{DIC}$ ranged from 1.6‰ to 2.47‰ over the same latitudinal range (30–60°S; but different longitude 150°W with slightly different oceanography; Figure 1a) compared to predicted 1.3–1.75‰ for the 1990s and predicted 1.1–1.55‰ in the 2000s (along 180° longitude, Figure 5b). The largest differences between the 1970s and 2000s are in the STSW, where the predicted $\delta^{13}C_{DIC}$ has declined by ~0.6–0.8‰, as a result of the Suess Effect, further enhanced by $\delta^{13}C_{air\text{-}sea}$ at these warm temperatures (Gruber et al., 1999; Lynch-Stieglitz et al., 1995; Schmittner et al., 2013). This is in close agreement with the estimated change in $\delta^{13}C_{DIC}$ expected by the Suess Effect of −0.020‰/year for latitudes 25–45°S between 1970s and 1990s (Gruber et al.,1999) and suggests that there have been no other major changes in biological productivity or ocean circulation over this time. There has been a smaller depletion in predicted $\delta^{13}C_{DIC}$ in the STF/SASW of ~0.5‰ between 1970s and 2000s, primarily as a result of the cooler temperatures, which increases the $\delta^{13}C_{air\text{-}sea}$. This reduction of 0.5‰ is just slightly higher than the estimated decline of −0.006‰/year for the Suess Effect between 45°S and 55°S between the 1970s and 1990s but within the error (Gruber et al., 1999). In contrast, there has been small changes (~0.2‰) in the $\delta^{13}C_{DIC}$ of the AASW (south of 50°S) over the last 40 years with $\delta^{13}C_{DIC}$ values around 1.6‰ during the 1970s (Quay et al., 1992) and predicted values of 1.4‰ in the 2000s (Figure 5b). Thus, the STSW are strongly influenced by biological productivity, but the predicted $\delta^{13}C_{DIC}$ pattern across the entire southwest Pacific is controlled by air-sea exchange of $CO_{2,}$ influenced by SST and residence times. The latter has resulted in a significant decline in the $\delta^{13}C_{DIC}$ as a result of the Suess Effect over the last 40 years. South of the PF, the predicted $\delta^{13}C_{DIC}$ of the AASW are primarily influenced by depleted $\delta^{13}C_{DIC}$ of the upwelling CDW in this region; thus, these high latitudes are predominantly controlled by circulation.

The estimated preindustrial $\delta^{13}C_{PI}$ is significantly higher than the modern predicted $\delta^{13}C_{DIC}$ in the southwest Pacific (Figures 4d and 5b). Olsen and Ninnemann (2010) describe the $\delta^{13}C_{PI}$ distribution as being "much richer and more detailed" than the modern $\delta^{13}C_{DIC}$ as a result of no overprinting by the Suess Effect (Olsen & Ninnemann, 2010; Quay et al., 2003; Schmittner et al., 2013; Sonnerup et al., 1999). These higher surface estimated $\delta^{13}C_{PI}$ values are similar to the $\delta^{13}C_{DIC}$ measured in the 1970s (Quay et al., 1992; Figure 5b) in the STSW but diverge significantly in the STF, SASW, and the AASW (Figure 5b). This significant difference between the estimated $\delta^{13}C_{PI}$ and the measured $\delta^{13}C_{DIC}$ south of 40°S suggests that the estimated $\delta^{13}C_{PI}$ values using the CFC method at these higher latitudes of the Southern Ocean are not correct. This is further supported by the lower core top $\delta^{13}C_{\textit{G.bulloides}TC}$ values (Figure 5b). Previous work has shown that the uptake of CFCs and anthropogenic CO_2 are different and dependent on the carbonate chemistry,

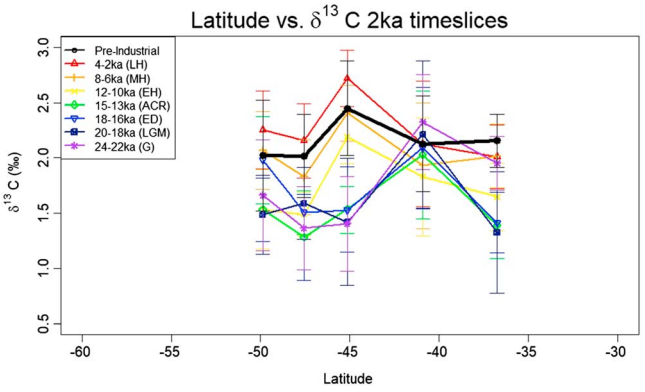

Figure 7. Latitude versus $\delta^{13}C_{G.bulloidesTC}$. For the core tops and 2-ka timeslice averages (24–22 ka—glacial [G = purple line]; 20–18 ka—last glacial maximum [LGM = dark blue line]; 18–16 ka—early deglacial [ED = blue line]; 15–13 ka—Antarctic Cold Reversal [ACR = green line]; 12–10 ka—early Holocene [EH = yellow line], 8–6 ka—mid-Holocene [MH = orange line], 4–2 ka—late Holocene [LH = red line], preindustrial/core tops [PI = black thick line]). Standard deviations for each timeslice are shown.

solubility, and the rate of air-sea gas exchange (McNeil et al., 2003). They showed that the CFC method overestimates the amount of anthropogenic carbon uptake in the Southern Ocean, especially in waters older than 30 years (Matear & McNeil, 2003; McNeil et al., 2003; Sonnerup, 2001). This suggests that the CFC method is not suitable for the high latitudes of the Southern Ocean, even at depths of ≥200 m. Additional methods to estimate the $\delta^{13}C$ change from anthropogenic carbon should be tested. It is also likely that with the reduction in atmospheric CFCs due to the Montreal Protocol, this CFC method may not be suitable for recent and future oceanographic data sets.

The core top average $\delta^{13}C_{G.bulloidesTC}$ values from the Monte Carlo simulation display considerable latitudinal differences across the New Zealand region (Figure 5b). Higher $\delta^{13}C_{G.bulloidesTC}$ values are found in low nutrient STSW of the southwest Pacific from 34–43°S, and two peaks are evident at ~45°S and ~50°S, likely reflecting the position of the highly productive STF to the south and east of New Zealand where the core tops are clustered (Figure 1; Bostock et al., 2015), thus crossing the STF twice. The latitudinal differences in the mean $\delta^{13}C_{G.bulloidesTC}$ values show close agreement with the $\delta^{13}C_{DIC}$ values from the 1970s (Quay et al., 1992) suggesting that they provide a good estimate of the late Holocene $\delta^{13}C_{DIC}$ in the southwest Pacific.

4.2. The $\delta^{13}C$ Variation Since the Last Glacial (25 kyr)

The core top $\delta^{13}C_{G.bulloidesTC}$ values (Figures 5a and 5b) provide a baseline to compare the downcore $\delta^{13}C_{G.bulloidesTC}$ data. With the temperature signal removed from the $\delta^{13}C_{G.bulloides}$ signal, any significant variation in the downcore $\delta^{13}C_{G.bulloidesTC}$ relative to these core top values can be inferred as a shift in the biological productivity, air-sea exchange, or ocean circulation (horizontally or vertically). The Monte Carlo simulated $\delta^{13}C_{G.bulloidesTC}$ data for the cores from the five regions in the southwest Pacific show large changes (up to 1.5‰) over the last 25 kyr (Figures 6b, 6d, 6f, 6h, and 6j and Figure 8a). There are some marked differences between the five regions, especially during the glacial to early deglaciation. The northern regions BOP and NCR show higher $\delta^{13}C_{G.bulloidesTC}$ values during the glacial than the other regions, but the values decline during the LGM and deglaciation, respectively. In contrast the southern regions (SCR, SolN, and SolS), which are strongly correlated with each other ($r > 0.7$; supporting information Table S4), all display relatively low $\delta^{13}C_{G.bulloidesTC}$ during the glacial and start to increase from 15 ka onward. From 12 ka onward, there is a general increasing trend in $\delta^{13}C_{G.bulloidesTC}$ values during the Holocene in all regions in this study.

The $\delta^{13}C_{G.bulloidesTC}$ from the different regions were plotted versus latitude for different 2-kyr time slices in order to discern major changes in the $\delta^{13}C_{G.bulloidesTC}$ patterns in the southwest Pacific since the last glacial (Figure 7). In the glacial time slice (24–22 ka) the highest values (>2‰) are in the northern regions (BOP and NCR); the lowest values are in the southern regions (SCR, SolN, and SolS) with ranges of 1.4–1.65‰. The values in the northern regions are within the standard deviation of the late Holocene, suggesting that there were similar biological productivity and oceanographic conditions in the STSW of the BOP with only a minor drop in SST (~1 °C lower than modern; Samson et al., 2005). In the NCR the $\delta^{13}C_{G.bulloidesTC}$ is higher than the late Holocene, although still within uncertainty (Figure 7), indicative of slightly higher biological productivity, which may have been the result of SASW leakage around either end of Chatham Rise contributing more nutrients to this region (Crundwell et al., 2008; Marr et al., 2013; Nelson et al., 2000). This is supported by high carbonate mass accumulation rates in core MD97-2121 during the glacial (Carter et al., 2000). On top of this glacial SST were significantly lower in the NCR (~4–6 °C lower than modern; Weaver et al., 1998; Nelson et al., 2000; Pahnke & Sachs, 2006), which would have increased the $\delta^{13}C_{air\text{-}sea}$ for this region. The southern regions all display low $\delta^{13}C_{G.bulloidesTC}$ during the glacial. There is evidence from SST proxies that the STF did not sit south of the South Island during the last glacial (Bostock et al., 2015) but remained topographically constrained to the Chatham Rise (Sikes et al., 2002; Weaver et al., 1998). Therefore, the SCR, SolN, and SolS regions were all overlain by glacial SASW. However, the glacial $\delta^{13}C$ was significantly lower than the core top and late Holocene $\delta^{13}C_{G.bulloidesTC}$ for SASW. This lower

signal may have been the result of significantly lower biological productivity in the SASW during the glacial, but recent work has suggested that the biological productivity was similar to, or only slightly lower than, the present in the Subantarctic region of the southwest Pacific (Durand et al., 2017). The $\delta^{13}C_{air\text{-}sea}$ should have been enhanced by the lower SST (~6 °C, 5–6 °C cooler than modern; Bostock et al., 2015; Pahnke & Sachs, 2006; Wells & Okada, 1997), so this is clearly overridden by other factors.

One explanation for the lower $\delta^{13}C_{G.bulloidesTC}$ in the glacial SASW is that the AASW penetrated further north than today. The glacial SASW SST of ~6 °C are characteristic of the PF in the modern ocean, where the $\delta^{13}C_{DIC}$ signal is lower (~1.5‰; Figure 4a). This is supported by similar $\delta^{13}C_{G.bulloidesTC}$ of ~1.5‰ from the PF core E11-2 in the central South Pacific ($\delta^{13}C_{G.bulloides}$ corrected using Mg/Ca SST estimates from *G. bulloides*; Mashiotta et al., 1999; Maxson, 2017; Ninnemann & Charles, 1997). Influx of AASW into the south of New Zealand is also supported by a larger percentage of the polar planktic nannofossil and foraminifera into the southern regions (SCR, SolN, and SolS), similar to south of the PF today (Bostock et al., 2015; Hayward et al., 2008; Nelson et al., 1993; Weaver et al., 1998; Wells and Okada, 1997). Stable isotope results from planktic foraminifera in the Subantarctic Zone of the South Atlantic have also suggested a very strong influence of polar waters and a salinity-driven density stratification, which would have resulted in a year-round isolation of the subsurface from the atmosphere, reducing the CO_2 release from the deep ocean and leading to a reduction in atmospheric CO_2 (Gottschalk et al., 2015). There is evidence for a more northerly position (up to 5° of latitude) of ACC fronts in other sectors of the Southern Ocean (reviewed in Kohfeld et al., 2013; Roberts et al., 2017), potentially influenced by the increased winter sea ice extent (Ferry et al., 2015; Gersonde et al., 2005) and northward shifts in the Southern Hemisphere Westerly Winds (SWW; Kohfeld et al., 2013).

Benthic carbon isotopes from *Cibicidoides wuellerstorfi* ($\delta^{13}C_{C.wuellerstorfi}$) from Antarctic Intermediate Water (AAIW) and Circumpolar Deep Waters (CDW) around southern New Zealand and Australia also display low values during the glacial and LGM (Moy et al., 2006; Pahnke & Zahn, 2005; Ronge et al., 2015). These CDW are the source waters for the AASW, while AAIW are sourced from the AASW, and there is a strong correlation between the $\delta^{13}C_{G.bulloidesTC}$ in the southern regions (SCR, SolN, and SolS) and the deep water $\delta^{13}C_{C.wuellerstorfi}$ over the last 25 ka ($r = 0.75$–0.96; supporting information Table S4).

During the LGM timeslice (20–18 ka) the latitudinal $\delta^{13}C_{G.bulloidesTC}$ pattern is similar to the glacial timeslice (Figure 7), with the exception that there is a large decrease (~0.5‰) in the $\delta^{13}C_{G.bulloidesTC}$ in the BOP region to values similar to the southern regions. Schiraldi et al. (2014) argue that this decline is not related to a reduction in biological productivity, as there is no evidence for changes in productivity (Wright et al., 1995). The decline occurs 2 kyr prior to a 0.3‰ decline in $\delta^{13}C$ of *Globoratalia inflata* (a thermocline species) from these same cores in the BOP. It also appears to be unrelated to the drop in $\delta^{13}C_{atm}$ from ice cores (Figure 8c; correlation coefficient $r = 0.6$; supporting information Table S4), which also occurs 2 kyr after the decline in $\delta^{13}C_{G.bulloidesTC}$ in the BOP (Schiraldi et al., 2014). Schiraldi et al. (2014) suggest that this significant change in $\delta^{13}C_{G.bulloidesTC}$ is related to a switch in the surface source waters from a cooler, fresher water to warmer STSW in the BOP. Warmer temperatures would have decreased the $\delta^{13}C_{air\text{-}sea}$. However, other evidence from foraminiferal assemblages and oxygen stable isotopes suggests that the Tasman Front was significantly further north during the LGM and did not shift to its current position at 32°S until the early Holocene at ~11 ka (Bostock et al., 2006; Martínez, 1997); thus, any increased STSW influx would not have been as warm as the modern currents in this region. Alternatively, the $\delta^{13}C_{G.bulloidesTC}$ may also be related to changes in the thickness of the mixed layer (Schiraldi et al., 2014). Thus, *G. bulloides*, which lives down to depths of 100 m today, may have been influenced by the lower $\delta^{13}C_{DIC}$ at thermocline depths. This increase in the depth of the mixed layer may have varied spatially in the region given the wide range (sd 0.55; Table 5) in $\delta^{13}C_{G.bulloidesTC}$ within the BOP region at this time (Figure 6a).

The low $\delta^{13}C_{G.bulloidesTC}$ at both the northern and southern ends of the transect (i.e., BoP and SolS) during the LGM suggest that there was both a strengthening of the South Pacific subtropical gyre in the north and an increased inflow of ACC to the south of the New Zealand region bringing in the lower $\delta^{13}C_{DIC}$ values in the northern STSW and south AASW (Figure 4). Recent climate modeling has that suggested such a scenario may have been possible with an increase in the South Pacific gyre from the weakening/merging of the modern two jet SWW structure (Subtropical and Polar jets) to a merged jet in the South Pacific (Chiang et al., 2018). This change in the SWW would have altered the wind stress curl, prompting a change in the surface

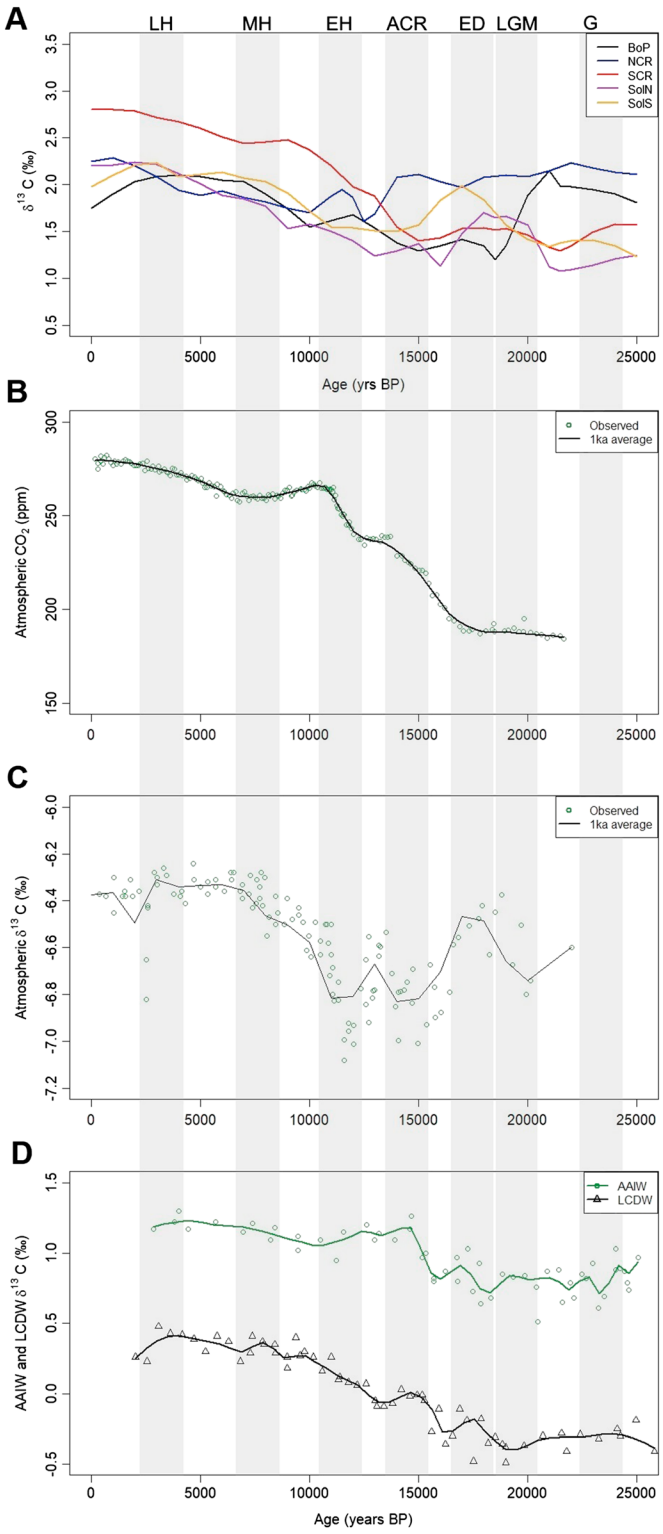

Figure 8. (a) Downcore temperature corrected $\delta^{13}C_{G.bull.}$ From all regions (BOP = Bay of Plenty; NCR = North Chatham Rise; SCR = South Chatham Rise; SolN = Solander Trough North; SolS = Solander Trough South. (b) Atmospheric CO_2 concentrations (Monnin et al., 2001), (c) EPICA ice core $\delta^{13}C_{atm}$ (Schmitt et al., 2012), and (d) benthic foraminifera $\delta^{13}C_{C.wuellerstorfi}$ levels for the last 25 kyr for GC34 (Moy et al., 2006) and SO136-003 (Ronge et al., 2015). Shaded regions in Figures 8a–8d correspond to timeslices in Figure 7. LH = late Holocene; MH = mid-Holocene; EH = early Holocene; ACR = Antarctic Cold Reversal; ED = early deglacial; LGM = last glacial maximum.

ocean circulation, (within the constraints of the complex topography in this region; Figure 1a). Consistent with this weaker split jet theory, there is evidence from SST proxies for a southward shift of the STF in the Solander Trough at the end of the LGM and early deglaciation (Bostock et al., 2015) resulting in a slight increase in $\delta^{13}C_{G.bulloides TC}$ in the SolN and SolS, although within uncertainty, as a result of increased biological productivity but no significant increase in $\delta^{13}C_{G.bulloides TC}$ in the SCR at this time, which continues to sit south of the STF (Figures 7 and 8a).

However, the $\delta^{13}C_{G.bulloides TC}$ values in the southern regions (SCR, SolN, Figures 7 and 8a) still remain low in the early deglaciation, counter to the expected $\delta^{13}C_{G.bulloides TC}$ values from the southward shift of the STF and warmer SST during the late LGM and early deglaciation (Bostock et al., 2015). The warmer SST of the STF should have increased the $\delta^{13}C_{air\text{-}sea,}$ and the increase in productivity associated with the STF over the Solander Trough (Durand et al., 2017) should have increased the $\delta^{13}C_{bio}$ and may explain the higher $\delta^{13}C_{G.bulloides TC}$ in the SolS. These anomalously low $\delta^{13}C_{G.bulloides TC}$ values during the early deglaciation corroborate previous work in the South Atlantic, South Pacific, and the tropical Pacific, which identified a dramatic decline in the planktic $\delta^{13}C_{foram}$ values at the start of the deglaciation. This drop in $\delta^{13}C_{foram}$ is proposed to be linked to the decrease in $\delta^{13}C_{atm}$ at this time (Figure 8c; Bostock et al., 2004; Ninnemann & Charles, 1997; Spero & Lea, 2002), resulting from the increased upwelling of ^{13}C depleted CO_2 to the atmosphere from the deep waters in the Southern Ocean (Figure 8b; Anderson et al., 2009; Gottschalk et al., 2015; Martínez-Botí et al., 2015). This indicates that the low $\delta^{13}C_{atm}$ values (Figure 8c) dramatically affected the $\delta^{13}C_{air\text{-}sea}$ at this time and is further supported by a minimum in both $\delta^{13}C_{atm}$ and $\delta^{13}C_{G.bulloides TC}$ in all the regions (except the NCR) at ~15 ka. There is a poor agreement ($r = 0.39$–0.57) between the $\delta^{13}C_{atm}$ from the EPICA ice core and the $\delta^{13}C_{G.bulloides TC}$ from the southern regions over the last 25 ka (supporting information Table S4), indicating that this influence may be for a limited period of time. Indeed, there is no decline in $\delta^{13}C_{G.bulloides TC}$ during the second $\delta^{13}C_{atm}$ decline between ~13 and 11 ka (Figures 8a and 8c; Lourantou et al., 2010). The influence of the low $\delta^{13}C_{atm,}$ however, is less clear in the northern regions (BOP and NCR), which may have been overridden by other factors.

During the ACR timeslice (15–13 ka) the $\delta^{13}C_{G.bulloides TC}$ values in all the southern regions remain low, similar to the glacial (24–22 ka) and the LGM (20–18 ka; Figure 7). The $\delta^{13}C_{G.bulloides TC}$ values in the NCR region during the ACR were higher than the other regions but slightly lower than the late Holocene, although within uncertainty. However, the cores in this zone all display significantly different $\delta^{13}C_{G.\ bulloides}$ values with MD97-2121 and CHAT 10K being high and the ODP site 1123 low and a large sd (0.58; Table 5); thus, the $\delta^{13}C_{G.bulloides TC}$ signal for this zone is heterogeneous at this time potentially related to different size fractions used. The relatively high $\delta^{13}C_{G.bulloides}$ values for MD97-2121 do not appear to be supported by high productivity during the ACR (Carter & Manighetti, 2006) but may be the result of increased mixed layer depth or upwelling as the $\delta^{13}C_{G.bulloides}$ values (and oxygen isotopes) of planktic foraminifera *Globigerinoides ruber* (shallow, subtropical species) and *Globoratalia inflata* (thermocline species) converge with the high $\delta^{13}C_{G.bulloides}$ (Carter et al., 2008). There is also evidence from SST estimates from Mg/Ca of *G. bulloides* and an increase in subpolar foraminiferal species in MD97-2121 of cooling during the ACR (Marr et al., 2013). Thus, the high $\delta^{13}C_{G.bulloides TC}$ in this region may be due to changes in the local circulation (SASW flowing through the Mernoo gap), increased wind mixing due to changes in the SWW split jet structure, and increased $\delta^{13}C_{air\text{-}sea}$ during the ACR. Pedro et al. (2016) used global climate model results to suggest that during the ACR the Southern Hemisphere winter Hadley Cell strengthens and shifts north due to the increased sea ice and changes in the Atlantic Meridional Overturning Circulation. This was potentially analogous to a negative Southern Annular Mode resulting in a strengthening of the South Pacific subtropical jet (Chiang et al., 2018), which may have increased the mixed layer depth and the $\delta^{13}C_{air\text{-}sea}$ in the NCR region.

The early Holocene (12–10 ka) is the first time that there is a significant change in the $\delta^{13}C_{G.bulloides TC}$ latitudinal transect (Figure 7), with a southward shift in the peak $\delta^{13}C_{G.bulloides TC}$ values from the NCR to the SCR region. In the SCR there is evidence for an increase in SST at MD97-2120 and DSDP 594 (Pahnke et al., 2003; Prebble et al., 2017) and higher biological productivity at core site DSDP 594 (Kowalski & Meyers, 1997), suggesting an increased influence of the STF south of the Chatham Rise in the early Holocene, possibly due to reduced SWW intensity over New Zealand (Prebble et al., 2017). The increase in the SST south of the STF (in the SCR, SolN, and SolS) would have also lead to an increase in the

$\delta^{13}C_{air\text{-}sea}$. At the same time the $\delta^{13}C_{G.bulloidesTC}$ values in the NCR declined to their lowest levels (1.8‰; Figure 6d), with low values in both MD97-2121 and CHAT10K (Figure 6c), despite the fact that productivity had peaked in MD97-2121 (Carter & Manighetti, 2006). Thus, this suggests that local oceanographic conditions had changed, possibly related to an increased influence of STSW inflow from the north due to the reinvigoration of the Tasman Front at ~11 ka (Bostock et al., 2006; Carter et al., 2008; Marr et al., 2013; Nelson et al., 2000). This is supported by increased numbers of subtropical foraminifera *G. ruber* in cores H214 (Samson et al., 2005) and MD97-2121 (Marr et al., 2013). This increase to significantly warmer subtropical SST would have also decreased the $\delta^{13}C_{air\text{-}sea}$ in the northern regions, similar to the modern situation (Figures 4a and 4b; Quay et al., 2009).

There is a slow and steady increase in $\delta^{13}C_{G.bulloidesTC}$ throughout the rest of the Holocene (post 10 ka) especially in the SCR. A similar steady increase in $\delta^{13}C_{G.bulloidesTC}$ is seen in the Subantarctic Zone of the South Atlantic during the Holocene (Gottschalk et al., 2015). The latitudinal pattern in $\delta^{13}C_{G.bulloidesTC}$ in the southwest Pacific remains the same throughout the Holocene (Figure 7) with the peak in $\delta^{13}C_{G.bulloidesTC}$ in the SCR region, similar to the preindustrial from core tops (Figure 5b). This suggests that the circulation (Bostock et al., 2015) and the productivity (Carter & Manighetti, 2006; Durand et al., 2017) have not changed significantly during the rest of the Holocene and have not impacted the $\delta^{13}C_{G.bulloidesTC}$ values in the southwest Pacific until the influence of the Suess Effect in the last century (King & Howard, 2004).

5. Conclusions

Using an MLR approach, we have developed new maps of the Austral spring spatial distribution of the estimated modern $\delta^{13}C_{DIC}$ for the southwest Pacific, which north of 60°S is driven by a combination of biological productivity and air-sea exchange. The pattern of $\delta^{13}C_{DIC}$, however, is most strongly driven by $\delta^{13}C_{air\text{-}sea}$ values that are highest between STF and the PF (42–60°S). South of the PF the $\delta^{13}C_{DIC}$ is dominated by the depleted $\delta^{13}C_{DIC}$ of the upwelling CDW. The $\delta^{13}C_{DIC}$ in the STSW are the most affected by the Suess Effect, with declines of 0.6–0.8‰ over the last 40 years. Smaller declines are evident in the STF/SASW, and no change is seen in the AASW. We attempt to remove the Suess Effect from the $\delta^{13}C_{DIC}$ using the CFC method to determine the preindustrial $\delta^{13}C_{PI}$. The $\delta^{13}C_{PI}$ is higher and displays a wider range but is overestimated in the Southern Ocean south of 40°S, where there is a considerable discrepancy between the $\delta^{13}C_{PI}$; $\delta^{13}C_{DIC}$ from the 1970s, 1990s, and 2000s; and (temperature corrected) $\delta^{13}C_{G.bulloidesTC}$ core top values.

The $\delta^{13}C_{G.bulloidesTC}$ from core tops from the southwest Pacific show a latitudinal gradient, with moderate values in the STSW, peaking at the biologically productive STF, and low values south of 50°S. Downcore $\delta^{13}C_{G.bulloidesTC}$ data show that during the glacial the values were high in the northern regions (BOP and NCR) and low for the southern regions (SCR, SolN, and SolS). A latitudinal transect shows a peak in $\delta^{13}C_{G.bulloidesTC}$ over the NCR region during the glacial and LGM. The low $\delta^{13}C_{G.bulloidesTC}$ in the southern regions is likely due to the inflow of very cold, low $\delta^{13}C_{DIC}$ AASW to the southern regions supported by SST and planktic foraminiferal assemblage data. This latitudinal pattern continues through the deglaciation, enhanced by the upwelling and release of low $\delta^{13}C_{DIC}$ from the Southern Ocean during the early deglaciation, until a major shift of the peak in $\delta^{13}C_{G.bulloidesTC}$ to the SCR region in the early Holocene. This is interpreted as a shift to higher $\delta^{13}C_{air\text{-}sea}$ values south of the STF with a warming of the SST in this region and also enhanced by a shift in the region of highest productivity to the SCR for the early Holocene. The changes in the oceanographic circulation in the southwest Pacific are likely linked to changes in the South Pacific SWW split jet structure. A weaker split jet in the LGM and early deglaciation enhances both the subtropical gyre and the inflow of waters from the Southern Ocean. The modern SWW split jet structure is likely established during the early Holocene.

Acknowledgments
We would like to thank Alix Post, Andrew Moy, Elisabeth Sikes, and Katharina Pahnke for providing $\delta^{13}C_{G.bulloides}$ core top and downcore data and Jean Lynch-Stieglitz for the provision of the Hudson-70 data set. We are grateful to Rolf Sonnerup, Joe Prebble, and Gavin Dunbar for their feedback during the project and for technical input using R and to Jennifer Hertzberg and an anonymous reviewer for their constructive comments on the manuscript. H. B. and the majority of the stable isotopes for the NIWA cores were funded by the New Zealand government funding of program COPR. This paper is a contribution to the Southern Hemisphere Assessment of PaleoEnvironments (SHAPE) program, supported by INQUA PALCOMM. The stable isotope data and age models are available on the Pangaea website.

References

Anderson, R., Ali, S., Bradtmiller, L., Nielsen, S., Fleisher, M., Anderson, B., & Burckle, L. (2009). Wind-driven upwelling in the Southern Ocean and the deglacial rise in atmospheric CO_2. *Science*, *323*(5920), 1443–1448. https://doi.org/10.1126/science.1167441

Bass, A. M., Munksgaard, N. C., O'Grady, D., Williams, M. J., Bostock, H. C., Rintoul, S. R., & Bird, M. I. (2014). Continuous shipboard measurements of oceanic $\delta^{18}O$, δD and $\delta^{13}C_{DIC}$ along a transect from New Zealand to Antarctica using cavity ring-down isotope spectrometry. *Journal of Marine Systems*, *137*, 21–27. https://doi.org/10.1016/j.jmarsys.2014.04.003

Bemis, B. E., Spero, H. J., Lea, D. W., & Bijma, J. (2000). Temperature influence on the carbon isotopic composition of *Globigerina bulloides* and *Orbulina universa* (planktonic foraminifera). *Marine Micropaleontology*, *38*(3–4), 213–228. https://doi.org/10.1016/S0377-8398(00)00006-2

Birch, H., Coxall, H. K., Pearson, P. N., Kroon, D., & O'Regan, M. (2013). Planktonic foraminifera stable isotopes and water column structure: Disentangling ecological signals. *Marine Micropaleontology*, *101*, 127–145. https://doi.org/10.1016/j.marmicro.2013.02.002

Bostock, H. C., Hayward, B. W., Neil, H. L., Sabaa, A. T., & Scott, G. H. (2015). Changes in the position of the subtropical front south of New Zealand since the last glacial period. *Paleoceanography*, *30*, 824–844. https://doi.org/10.1002/2014PA002652

Bostock, H. C., Opdyke, B., Gagan, M., Kiss, A., & Fifield, L. K. (2006). Glacial/interglacial changes in the East Australian current. *Climate Dynamics*, *26*(6), 645–659. https://doi.org/10.1007/s00382-005-0103-7

Bostock, H. C., Opdyke, B. N., Gagan, M. K., & Fifield, L. K. (2004). Carbon isotope evidence for changes in Antarctic Intermediate Water circulation and ocean ventilation in the southwest Pacific during the last deglaciation. *Paleoceanography*, *19*, PA4013. https://doi.org/10.1029/2004PA001047

Broecker, W. S., & Maier-Reimer, E. (1992). The influence of air-sea exchange on the carbonate isotope distribution in the sea. *Global Biogeochemical Cycles*, *6*(3), 315–320. https://doi.org/10.1029/92GB01672

Butzin, M., Prange, M., & Lohmann, G. (2005). Radiocarbon simulations for the glacial ocean: The effects of wind stress, Southern Ocean sea ice and Heinrich events. *Earth and Planetary Science Letters*, *235*(1–2), 45–61. https://doi.org/10.1016/j.epsl.2005.03.003

Carter, L., & Manighetti, B. (2006). Glacial/interglacial control of terrigenous and biogenic fluxes in the deep ocean off a high input, collisional margin: A 139 kyr-record from New Zealand. *Marine Geology*, *226*(3–4), 307–322. https://doi.org/10.1016/j.margeo.2005.11.004

Carter, L., Manighetti, B., Ganssen, G., & Northcote, L. (2008). Southwest Pacific modulation of abrupt climate change during the Antarctic Cold Reversal-Younger Dryas. *Palaeogeography, Palaeoclimatology, Palaeoecology*, *260*(1–2), 284–298. https://doi.org/10.1016/j.palaeo.2007.08.013

Carter, L., Neil, H., & McCave, I. (2000). Glacial to interglacial changes in non-carbonate and carbonate accumulation in the SW Pacific Ocean, New Zealand. *Palaeogeography, Palaeoclimatology, Palaeoecology*, *162*(3–4), 333–356. https://doi.org/10.1016/S0031-0182(00)00137-1

Carter, R. M., & Gammon, P. (2004). New Zealand maritime glaciation: millennial-scale southern climate change since 3.9 Ma. *Science*, *304*(5677), 1659–1662.

Charles, C. D., & Fairbanks, R. G. (1990). Glacial to interglacial changes in the isotopic gradients of Southern Ocean surface water. In *Geological History of the Polar Oceans: Arctic Versus Antarctic*, (pp. 519–538). Dordrecht: Springer.

Charles, C. D., Lynch-Stieglitz, J., Ninnemann, U. S., & Fairbanks, R. G. (1996). Climate connections between the hemisphere revealed by deep sea sediment core/ice core correlations. *Earth and Planetary Science Letters*, *142*(1-2), 19–27. https://doi.org/10.1016/0012-821X(96)00083-0

Chiang, J. C., Tokos, K., Lee, S. Y., & Matsumoto, K. (2018). Contrasting impacts of the South Pacific Split Jet and the Southern Annular Mode modulation on Southern Ocean circulation and biogeochemistry. *Paleoceanography and Paleoclimatology*, *33*, 2–20. https://doi.org/10.1002/2017PA003229

Chiswell, S. M., Bostock, H. C., Sutton, P. J., & Williams, M. J. (2015). Physical oceanography of the deep seas around New Zealand: A review. *New Zealand Journal of Marine and Freshwater Research*, *49*(2), 286–317. https://doi.org/10.1080/00288330.2014.992918

Crundwell, M., Scott, G., Naish, T., & Carter, L. (2008). Glacial-interglacial ocean climate variability from planktonic foraminifera during the Mid-Pleistocene transition in the temperate Southwest Pacific, ODP Site 1123. *Palaeogeography, Palaeoclimatology, Palaeoecology*, *260*(1-2), 202–229. https://doi.org/10.1016/j.palaeo.2007.08.023

Duncan, B., Carter, L., Dunbar, G., Bostock, H., Neil, H., Scott, G., Hayward, B.W., & Sabaa, A. (2016). Interglacial/glacial changes in coccolith-rich deposition in the SW Pacific Ocean: An analogue for a warmer world? *Global and Planetary Change*, *144*, 252–262.

Durand, A., Chase, Z., Noble, T. L., Bostock, H., Jaccard, S. L., Kitchener, P., et al. (2017). Export production in the New-Zealand region since the Last Glacial Maximum. *Earth and Planetary Science Letters*, *469*, 110–122. https://doi.org/10.1016/j.epsl.2017.03.035

Eide, M., Olsen, A., Ninnemann, U. S., & Eldevik, T. (2017). A global estimate of the full oceanic ^{13}C Suess effect since the preindustrial. *Global Biogeochemical Cycles*, *31*, 492–514. https://doi.org/10.1002/2016GB005472

Eide, M., Olsen, A., Ninnemann, U. S., & Johannessen, T. (2017). A global ocean climatology of preindustrial and modern ocean $\delta^{13}C$. *Global Biogeochemical Cycles*, *31*, 515–534. https://doi.org/10.1002/2016GB005473

Elderfield, H., Vautravers, M., & Cooper, M. (2002). The relationship between shell size and Mg/Ca, Sr/Ca, $\delta^{18}O$, and $\delta^{13}C$ of species of planktonic foraminifera. *Geochemistry, Geophysics, Geosystems*, *3*(8), 1052. https://doi.org/10.1029/2001GC000194

Ferry, A. J., Crosta, X., Quilty, P. G., Fink, D., Howard, W., & Armand, L. K. (2015). First records of winter sea ice concentration in the southwest Pacific sector of the Southern Ocean. *Paleoceanography*, *30*, 1525–1539. https://doi.org/10.1002/2014PA002764

Gersonde, R., Crosta, X., Abelmann, A., & Armand, L. (2005). Sea-surface temperature and sea ice distribution of the Southern Ocean at the EPILOG Last Glacial Maximum—A circum-Antarctic view based on siliceous microfossil records. *Quaternary Science Reviews*, *24*(7-9), 869–896. https://doi.org/10.1016/j.quascirev.2004.07.015

Gottschalk, J., Skinner, L. C., & Waelbroeck, C. (2015). Contribution of seasonal sub-Antarctic surface water variability to millennial-scale changes in atmospheric CO_2 over the last deglaciation and Marine Isotope Stage 3. *Earth and Planetary Science Letters*, *411*, 87–99. https://doi.org/10.1016/j.epsl.2014.11.051

Graham, R. M., & de Boer, A. M. (2013). The dynamical subtropical front. *Journal of Geophysical Research: Oceans*, *118*, 5676–5685. https://doi.org/10.1002/jgrc.20408

Gruber, N., Keeling, C. D., Bacastow, R. B., Guenther, P. R., Lueker, T. J., Wahlen, M., et al. (1999). Spatiotemporal patterns of carbon-13 in the global surface oceans and the oceanic Suess effect. *Global Biogeochemical Cycles*, *13*(2), 307–335. https://doi.org/10.1029/1999GB900019

Hamilton, L. J. (2006). Structure of the Subtropical Front in the Tasman Sea. *Deep-Sea Research Part I*, *53*(12), 1989–2009. https://doi.org/10.1016/j.dsr.2006.08.013

Hayward, B. W., Scott, G. H., Crundwell, M. P., Kennett, J. P., Carter, L., Neil, H. L., et al. (2008). The effect of submerged plateaux on Pleistocene gyral circulation and sea-surface temperatures in the Southwest Pacific. *Global and Planetary Change*, *63*(4), 309–316. https://doi.org/10.1016/j.gloplacha.2008.07.003

Hodell, D. A., Charles, C. D., & Ninnemann, U. S. (2000). Comparison of interglacial stages in the South Atlantic sector of the Southern Ocean for the past 450 kyr: Implifications for Marine Isotope Stage (MIS) 11. *Global and Planetary Change*, *24*(1), 7–26. https://doi.org/10.1016/S0921-8181(99)00069-7

Keeling, C. D. (1979). The Suess effect: 13Carbon-14Carbon interrelations. *Environment International*, *2*(4–6), 229–300.
Keir, R., Rehder, G., & Suess, E. (1998). The $\delta^{13}C$ anomaly in the northeastern Atlantic. *Global Biogeochemical Cycles*, *12*(3), 467–477. https://doi.org/10.1029/98GB02054
Khider, D., Ahn, S., Lisiecki, L. E., Lawrence, C. E., & Kienast, M. (2017). The role of uncertainty in estimating lead/lag relationships in marine sedimentary archives: A case study from the tropical Pacific. *Paleoceanography*, *32*, 1275–1290. https://doi.org/10.1002/2016PA003057
King, A. L., & Howard, W. R. (2001). Seasonality of foraminiferal flux in sediment traps at Chatham rise, SW Pacific: Implications for paleotemperature estimates. *Deep-Sea Research Part I*, *48*(7), 1687–1708. https://doi.org/10.1016/S0967-0637(00)00106-0
King, A. L., & Howard, W. R. (2004). Planktonic foraminiferal $\delta^{13}C$ records from Southern Ocean sediment traps: New estimates of the oceanic Suess effect. *Global Biogeochemical Cycles*, *18*, GB2007. https://doi.org/10.1029/2003GB002162
Ko, Y. H., Lee, K., Quay, P. D., & Feely, R. A. (2014). Decadal (1994–2008) change in the carbon isotope ratio in the eastern South Pacific Ocean, Global Biogeochem. *Cycles*, *28*, 775–785. https://doi.org/10.1002/2013GB004786
Kohfeld, K. E., Anderson, R. F., & Lynch-Stieglitz, J. (2000). Carbon isotopic disequilibrium in polar planktonic foraminifera and its impact on modern and Last Glacial Maximum reconstructions. *Paleoceanography*, *15*(1), 53–64. https://doi.org/10.1029/1999PA900049
Kohfeld, K. E., Graham, R. M., de Boer, A. M., Sime, L. C., Wolff, E. W., Le Quere, C., & Bopp, L. (2013). Southern hemisphere westerly wind changes during the Last Glacial Maximum: Paleo-data synthesis. *Quaternary Science Reviews*, *68*, 76–95. https://doi.org/10.1016/j.quascirev.2013.01.017
Kowalski, E. A., & Meyers, P. A. (1997). Glacial–interglacial variations in Quaternary production of marine organic matter at DSDP Site 594, Chatham Rise, southeastern New Zealand margin. *Marine Geology*, *140*(3-4), 249–263. https://doi.org/10.1016/S0025-3227(97)00044-3
Kroopnick, P. (1985). The distribution of ^{13}C of ΣCO_2 in the world oceans. *Deep Sea Research Part A. Oceanographic Research Papers*, *32*(1), 57–84. https://doi.org/10.1016/0198-0149(85)90017-2
Lisiecki, L. E., & Raymo, M. E. (2005). A Pliocene-Pleistocene stack of 57 globally distributed benthic $\delta^{18}O$ records. *Paleoceanography*, *20*, PA1003. https://doi.org/10.1029/2004PA001071
Lourantou, A., Lavrič, J. V., Köhler, P., Barnola, J.-M., Paillard, D., Michel, E., et al. (2010). Constraint of the CO_2 rise by new atmospheric carbon isotopic measurements during the last deglaciation. *Global Biogeochemical Cycles*, *24*, GB2015. https://doi.org/10.1029/2009GB003545
Lynch-Stieglitz, J., & Fairbanks, R. G. (1994). A conservative tracer for glacial ocean circulation from carbon isotope and palaeo-nutrient measurements in benthic foraminifera. *Nature*, *369*(6478), 308–310. https://doi.org/10.1038/369308a0
Lynch-Stieglitz, J., Stocker, T. F., Broecker, W. S., & Fairbanks, R. G. (1995). The influence of air-sea exchange on the isotopic composition of oceanic carbon: Observations and modeling. *Global Biogeochemical Cycles*, *9*(4), 653–665. https://doi.org/10.1029/95GB02574
Marr, J. P., Carter, L., Bostock, H. C., Bolton, A., & Smith, E. (2013). Southwest Pacific Ocean response to a warming world: Using Mg/Ca, Zn/Ca, and Mn/Ca in foraminifera to track surface ocean water masses during the last deglaciation. *Paleoceanography*, *28*, 347–362. https://doi.org/10.1002/palo.20032
Martínez, R. J. (1997). Decreasing influence of Subantarctic Mode Water north of the Tasman Front over the past 150 kyr. *Palaeogeography, Palaeoclimatology, Palaeoecology*, *131*(3–4), 355–364. https://doi.org/10.1016/S0031-0182(97)00011-4
Martínez-Botí, M. A., Marino, G., Foster, G. L., Ziveri, P., Henehan, M. J., Rae, J. W., et al. (2015). Boron isotope evidence for oceanic carbon dioxide leakage during the last deglaciation. *Nature*, *518*(7538), 219–222. https://doi.org/10.1038/nature14155
Mashiotta, T. A., Lea, D. W., & Spero, H. J. (1999). Glacial–interglacial changes in Subantarctic sea surface temperature and $\delta^{18}O$-water using foraminiferal Mg. *Earth and Planetary Science Letters*, *170*(4), 417–432. https://doi.org/10.1016/S0012-821X(99)00116-8
Matear, R., & McNeil, B. (2003). Decadal accumulation of anthropogenic CO_2 in the Southern Ocean: A comparison of CFC-age derived estimates to multiple-linear regression estimates. *Global Biogeochemical Cycles*, *17*(4), 1113. https://doi.org/10.1029/2003GB002089
Maxson, C. (2017). Carbon isotopic equilibrium of the surface waters as a proxy for climate change through the last glacial/interglacial cycle in the Southwest Pacific. Unpublished MSc thesis, Victoria University, Wellington, New Zealand. http://researcharchive.vuw.ac.nz/handle/10063/6417
McCave, I. N., Carter, L., & Hall, I. R. (2008). Glacial–interglacial changes in water mass structure and flow in the SW Pacific Ocean. *Quaternary Science Reviews*, *27*(19–20), 1886–1908.
McNeil, B., Matear, R., & Tilbrook, B. (2001). Does carbon 13 track anthropogenic CO_2 in the Southern Ocean? *Global Biogeochemical Cycles*, *15*(3), 597–613. https://doi.org/10.1029/2000GB001352
McNeil, B. I., Matear, R. J., Key, R. M., Bullister, J. L., & Sarmiento, J. L. (2003). Anthropogenic CO_2 uptake by the ocean based on the global chlorofluorocarbon data set. *Science*, *299*(5604), 235–239. https://doi.org/10.1126/science.1077429
Monnin, E., Indermühle, A., Dällenbach, A., Flückiger, J., Stauffer, B., Stocker, T. F., et al. (2001). Atmospheric CO_2 concentrations over the last glacial termination. *Science*, *291*(5501), 112–114. https://doi.org/10.1126/science.291.5501.112
Mook, W., Bommerson, J., & Staverman, W. (1974). Carbon isotope fractionation between dissolved bicarbonate and gaseous carbon dioxide. *Earth and Planetary Science Letters*, *22*(2), 169–176. https://doi.org/10.1016/0012-821X(74)90078-8
Mook, W. G. (1986). 13C in atmospheric CO_2. *Netherlands Journal of Sea Research*, *20*(2-3), 211–223.
Moy, A. D., Howard, W. R., & Gagan, M. K. (2006). Late Quaternary palaeoceanography of the circumpolar deep water from the South Tasman Rise. *Journal of Quaternary Science*, *21*(7), 763–777. https://doi.org/10.1002/jqs.1067
Neil, H. L. (1997). Late Quaternary variability of surface and relationships in upper Quaternary sediments of the eastern deep water masses — Chatham Rise, SW Pacific. D.Phil. Thesis, *University of Waikato*, Hamilton, New Zealand.
Neil, H. L., Carter, L., & Morris, M. Y. (2004). Thermal isolation of Campbell Plateau, New Zealand, by the Antarctic Circumpolar Current over the past 130 kyr. *Paleoceanography*, *19*, PA4008. https://doi.org/10.1029/2003PA000975
Nelson, C., Hendy, I., Neil, H., Hendy, C., & Weaver, P. (2000). Last glacial jetting of cold waters through the Subtropical Convergence zone in the Southwest Pacific off eastern New Zealand, and some geological implications. *Palaeogeography, Palaeoclimatology, Palaeoecology*, *156*(1-2), 103–121. https://doi.org/10.1016/S0031-0182(99)00134-0
Nelson, C. S., Cooke, P. J., Hendy, C. H., & Cuthbertson, A. M. (1993). Oceanographic and climatic changes over the past 160,000 years at Deep Sea Drilling Project Site 594 off southeastern New Zealand, southwest Pacific Ocean. *Paleoceanography*, *8*(4), 435–458. https://doi.org/10.1029/93PA01162
Ninnemann, U. S., & Charles, C. D. (1997). Regional differences in Quaternary Subantarctic nutrient cycling: Link to intermediate and deep water ventilation. *Paleoceanography*, *12*(4), 560–567. https://doi.org/10.1029/97PA01032
Olsen, A., & Ninnemann, U. (2010). Large $\delta^{13}C$ gradients in the preindustrial North Atlantic revealed. *Science*, *330*(6004), 658–659. https://doi.org/10.1126/science.1193769
Pahnke, K., & Sachs, J. P. (2006). Sea surface temperatures of southern midlatitudes 0–160 kyr BP. *Paleoceanography*, *21*, PA2003. https://doi.org/10.1029/2005PA001191

Pahnke, K., & Zahn, R. (2005). Southern Hemisphere water mass conversion linked with North Atlantic climate variability. *Science*, *307*(5716), 1741–1746. https://doi.org/10.1126/science.1102163

Pahnke, K., Zahn, R., Elderfield, H., & Schulz, M. (2003). 340,000-year centennial-scale marine record of Southern Hemisphere climatic oscillation. *Science*, *301*(5635), 948–952. https://doi.org/10.1126/science.1084451

Pedro, J. B., Bostock, H. C., Bitz, C. M., He, F., Vandergoes, M. J., Steig, E. J., et al. (2016). The spatial extent and dynamics of the Antarctic Cold Reversal. *Nature Geoscience*, *9*(1), 51–55. https://doi.org/10.1038/NGEO2580

Prebble, J., Bostock, H., Cortese, G., Lorrey, A., Hayward, B., Calvo, E., et al. (2017). Evidence for a Holocene Climatic Optimum in the Southwest Pacific: A multiproxy study. *Paleoceanography*, *32*, 763–779. https://doi.org/10.1002/2016PA003065

Prebble, J. G., Crouch, E. M., Carter, L., Cortese, G., Bostock, H., & Neil, H. (2013). An expanded modern dinoflagellate cyst dataset for the Southwest Pacific and Southern hemisphere with environmental associations. *Mar. Micropal.*, *101*, 33–48. https://doi.org/10.1016/j.marmicro.2013.04.004

Quay, P., Sonnerup, R., Westby, T., Stutsman, J., & McNichol, A. (2003). Changes in the $^{13}C/^{12}C$ of dissolved inorganic carbon in the ocean as a tracer of anthropogenic CO_2 uptake. *Global Biogeochemical Cycles*, *17*(1), 1004. https://doi.org/10.1029/2001GB001817

Quay, P., Sonnerup, R., Stutsman, J., Maurer, J., Körtzinger, A., Padin, X. A., & Robinson, C. (2007). Anthropogenic CO_2 accumulation rates in the North Atlantic Ocean from changes in the 13C/12C of dissolved inorganic carbon. *Global biogeochemical cycles*, *21*(1).

Quay, P., Tilbrook, B., & Wong, C. (1992). Oceanic uptake of fossil fuel CO_2: Carbon-13 evidence. *Science*, *256*(5053), 74–79. https://doi.org/10.1126/science.256.5053.74

Quay, P. D., Stutsman, J., Feely, R. A., & Juranek, L. W. (2009). Net community production rates across the subtropical and equatorial Pacific Ocean estimated from air-sea $\delta^{13}C$ disequilibrium. *Global Biogeochemical Cycles*, *23*, GB2006. https://doi.org/10.1029/2008GB003193

Reimer, P. J., Bard, E., Bayliss, A., Beck, J. W., Blackwell, P. G., Ramsey, C. B., et al. (2013). IntCal13 and Marine13 radiocarbon age calibration curves 0–50,000 years cal BP. *Radiocarbon*, *55*(04), 1869–1887. https://doi.org/10.2458/azu_js_rc.55.16947

Roberts, J., McCave, I. N., McClymont, E. L., Kender, S., Hillenbrand, C.-D., Matano, R., et al. (2017). Deglacial changes in flow and frontal structure through the Drake Passage. *Earth and Planetary Science Letters*, *474*, 397–408. https://doi.org/10.1016/j.epsl.2017.07.004

Ronge, T. A., Steph, S., Tiedemann, R., Prange, M., Merkel, U., Nürnberg, D., & Kuhn, G. (2015). Pushing the boundaries: Glacial/interglacial variability of intermediate and deep waters in the southwest Pacific over the last 350,000 years. *Paleoceanography*, *30*, 23–38. https://doi.org/10.1002/2014PA002727

Sabine, C. L., Feely, R. A., Gruber, N., Key, R. M., Lee, K., Bullister, J. L., et al. (2004). The oceanic sink for anthropogenic CO_2. *Science*, *305*(5682), 367–371. https://doi.org/10.1126/science.1097403

Samson, C. R., Sikes, E. L., & Howard, W. R. (2005). Deglacial paleoceanographic history of the Bay of Plenty, New Zealand. *Paleoceanography*, *20*, PA4017. https://doi.org/10.1029/2004PA001088

Schiraldi, B., Sikes, E. L., Elmore, A. C., Cook, M. S., & Rose, K. A. (2014). Southwest Pacific subtropics responded to last deglacial warming with changes in shallow water sources. *Paleoceanography*, *29*, 595–611. https://doi.org/10.1002/2013PA002584

Schlitzer, R. (2009). *Ocean Data View Software*. http://odv.awi.de/.

Schmitt, J., Schneider, R., Elsig, J., Leuenberger, D., Lourantou, A., Chappellaz, J., et al. (2012). Carbon isotope constraints on the deglacial CO_2 rise from ice cores. *Science*, *336*(6082), 711–714. https://doi.org/10.1126/science.1217161

Schmittner, A., Gruber, N., Mix, A., Key, R., Tagliabue, A., & Westberry, T. (2013). Biology and air–sea gas exchange controls on the distribution of carbon isotope ratios ($\delta^{13}C$) in the ocean. *Biogeosciences*, *10*(9), 5793–5816. https://doi.org/10.5194/bg-10-5793-2013

Sikes, E., Howard, W., Neil, H., & Volkman, J. (2002). Glacial-interglacial sea surface temperature changes across the subtropical front east of New Zealand based on alkenone unsaturation ratios and foraminiferal assemblages. *Paleoceanography*, *17*(2), 1012. https://doi.org/10.1029/2001PA000640

Smith, R. O., Vennell, R., Bostock, H. C., & Williams, M. J. (2013). Interaction of the subtropical front with topography around southern New Zealand. *Deep Sea Research Part I: Oceanographic Research Papers*, *76*, 13–26. https://doi.org/10.1016/j.dsr.2013.02.007

Sokolov, S., & Rintoul, S. R. (2009a). Circumpolar structure and distribution of the Antarctic Circumpolar Current fronts: 1. Mean circumpolar paths. *Journal of Geophysical Research*, *114*, C11018. https://doi.org/10.1029/2008JC005108

Sokolov, S., & Rintoul, S. R. (2009b). Circumpolar structure and distribution of the Antarctic Circumpolar Current fronts: 2. Variability and relationship to sea surface height. *Journal of Geophysical Research*, *114*, C11019. https://doi.org/10.1029/2008JC005248

Sonnerup, R. E. (2001). On the relations among CFC derived water mass ages. *Geophysical Research Letters*, *28*(9), 1739–1742. https://doi.org/10.1029/2000GL012569

Sonnerup, R. E., Quay, P. D., McNichol, A. P., Bullister, J. L., Westby, T. A., & Anderson, H. L. (1999). Reconstructing the oceanic ^{13}C Suess effect. *Global Biogeochemical Cycles*, *13*(4), 857–872. https://doi.org/10.1029/1999GB900027

Spero, H. J., Bijma, J., Lea, D. W., & Bemis, B. E. (1997). Effect of seawater carbonate concentration on foraminiferal carbon and oxygen isotopes. *Nature*, *390*(6659), 497–500. https://doi.org/10.1038/37333

Spero, H. J., & Lea, D. W. (1996). Experimental determination of stable isotope variability in *Globigerina bulloides*: Implications for paleoceanographuc reconstructions. *Marine Micropaleontology*, *28*(3-4), 231–246. https://doi.org/10.1016/0377-8398(96)00003-5

Spero, H. J., & Lea, D. W. (2002). The cause of carbon isotope minimum events on glacial terminations. *Science*, *296*(5567), 522–525. https://doi.org/10.1126/science.1069401

Tomczak, M., & Godfrey, J. S. (1994). *Regional oceanography: An introduction* (Vol. 660, pp. 10,591–15,153). Pergamon, Oxford: elsevier science ltd.

Weaver, P. P. E., Carter, L., & Neil, H. L. (1998). Response of surface water masses and circulation to late Quaternary climate change east of New Zealand. *Paleoceanography*, *13*(1), 70–83. https://doi.org/10.1029/97PA02982

Weaver, P. P. E., Neil, H., & Carter, L. (1997). Sea surface temperature estimates from the Southwest Pacific based on planktonic foraminifera and oxygen isotopes. *Palaeogeography, Palaeoclimatology, Palaeoecology*, *131*(3–4), 241–256.

Wells, P., & Okada, H. (1997). Response of nannoplankton to major changes in sea-surface temperature and movements of hydrological fronts over Site DSDP 594 (south Chatham Rise, southeastern New Zealand), during the last 130 kyr. *Marine Micropaleontology*, *32*(3–4), 341–363.

World Ocean Atlas (2013). https://www.nodc.noaa.gov/OC5/woa13/

Wright, I. C., McGlone, M. S., Nelson, C. S., & Pillans, B. J. (1995). An integrated latest Quaternary (stage 3 to present) paleoclimatic and paleoceanographic record from offshore northern New Zealand. *Quaternary Research*, *44*(02), 283–293. https://doi.org/10.1006/qres.1995.1073

Zhang, J., Quay, P., & Wilbur, D. (1995). Carbon isotope fractionation during gas-water exchange and dissolution of CO_2. *Geochimica et Cosmochimica Acta*, *59*(1), 107–114. https://doi.org/10.1016/0016-7037(95)91550-D